dx.doi.org/10.22093/wwj.2022.379990.3314

Original Paper

Journal of Water and Wastewater, Vol. 33, No. 6, pp: 67-92

Removal of Pb(II) from Aqueous Solutions Using Magnetic Mesoporous Silica Nanocomposites: Modeling and Optimization Based on Response Surface Methodology

Sh. Emrani[1], M. Ebrahimi[2], R. Zhiani[3], A. R. Motavalizadehkakhky[3]

1. PhD. Student, Dept. of Chemistry, Mashhad Branch, Islamic Azad University, Mashhad, Iran
2. Assoc. Prof., Dept. of Chemistry, Mashhad Branch, Islamic Azad University, Mashhad, Iran
(Corresponding Author) ebrachem2007@yahoo.com
3. Assoc. Prof., Dept. of Chemistry, Neyshabur Branch, Islamic Azad University, Neyshabur, Iran
and Advanced Research Center of Chemistry Biochemistry & Nanomaterial, Neyshabur Branch, Islamic Azad University, Neyshabur, Iran

(Received Jan. 7, 2023 Accepted March 1, 2023)

To cite this article:
Emrani, Sh., Ebrahimi, M., Zhiani, R., Motavalizadehkakhky, A. R. 2023. "Removal of Pb(II) from aqueous solutions using magnetic mesoporous silica nanocomposites: modeling and optimization based on response surface methodology" Journal of Water and Wastewater, 33(6), 67-92. Doi: 10.22093/wwj.2022.379990.3314.

Abstract

In the adsorption process of heavy metals, a major challenge is to design and develop adsorbent materials in an abundance of accessible adsorption sites with high affinity to achieve both fast adsorption kinetics and increased adsorption capacity for toxic contaminants. The removal of pollutants by mesoporous silica adsorbents is now in the limelight due to the nontoxicity and biocompatibility of these materials with the environment. In this study, a fibrous core-shell magnetic mesoporous composite ($Fe_3O_4/SiO_2/KCC^{-1}$) was successfully synthesized and used as a nano-adsorbent to remove Pb(II) from an aqueous solution. The adsorbent was characterized by employing TEM, SEM, FTIR, VSM, XRD, and N^2 adsorption–desorption techniques. According to the results, $Fe_3O_4/SiO_2/KCC^{-1}$ was successfully synthesized with an average pore diameter of 7.94 nm, a surface area of 813.07 m^2 g^{-1}, and a pore volume of 1.41 cm^3 g^{-1}. The response surface methodology (RSM) was then adopted in the central composite design (CCD) to optimize parameters of the adsorption process. The optimal conditions for Pb(II) adsorption were then determined at a temperature of 80 °C, an adsorption dosage of 0.04 g L^{-1}, a pH 5.6, and the contact time of 38 min. The removal rate of Pb(II) was 90%. Studies of equilibrium and kinetics indicated that the adsorption process followed Langmuir's isotherm and the pseudo-first-order model with correlation coefficients of 0.98 and 0.99, respectively. The maximum adsorption capacity of $Fe_3O_4/SiO_2/KCC^{-1}$ was reported 574.4 mg g^{-1}. Moreover, the thermodynamic parameters known as enthalpy ($\Delta H° = +5.84$ kJ mol^{-1}), negative Gibbs free energy ($\Delta G°$) values, and entropy ($\Delta S° = +23.42$ kJ mol^{-1} K^{-1}) indicated that the adsorption was endothermic and spontaneous with the increased disorder at the solid–liquid interphase.

Keywords: Magnetic Mesoporous Adsorbent, Central Composite Design, Isotherm, Kinetics, Thermodynamics.

1. Introduction

Water pollution with heavy metal ions is still a worldwide threat to the public health because of high toxicity and non-biodegradability (Wu et al., 2019). Known as a common contaminant of industrial wastewater, lead is considered a very toxic element (Wang et al., 2018). According to the standards announced by the World Health Organization, the maximum allowed concentration of lead in drinking water is 0.01 mg L^{-1}, whereas its maximum limit for discharge in wastewater is 0.1 mg L^{-1} (Betiha et al., 2020). The concentrations of lead above the threshold of toxicity may cause human health problems such as kidney or liver failure, insomnia, central nervous system damage, hallucinations, anemia, and irritability (Faraji-Khiavi et al., 2022).

Therefore, it is necessary to find effective solutions to the removal of these pollutants from water sources and the implementation of water purification appropriate treatment. Recently, various physical and chemical methods have been developed for the removal of heavy metals, adsorption (Fooladgar et al., 2019), chemical precipitation (Cheng et al., 2022), coagulation–flocculation (Moghaddam et al., 2010), ion exchange (Liu et al., 2021), flotation (Cheng et al., 2022), reverse osmosis (Taseidifar et al., 2019), electrochemical methods (Anantha et al., 2020), membrane filtration (Vieira et al., 2020), solvent extraction (Sun et al., 2020), and biological processes (Dhaliwal et al., 2020).

Each of these methods has certain advantages and disadvantages based on simplicity, flexibility, process efficiency, cost efficiency, time consumption, repeatability, and environmental friendliness. The adsorption technique is preferred to other methods for treatment purposes in terms of flexibility, low costs, simple design, less sludge production, high effectiveness, insensitivity to the resultant toxic materials, and desirable outputs (Nasab et al., 2019).

According to the research literature, various nanostructured adsorbent substances were utilized to remove heavy metal ions from aquatic environments such as the activated carbon (Clifford et al., 1986), mesoporous silica (Da'na and Sayari, 2012), low-cost natural lignocelluloses substrates (Šćiban et al., 2006), zeolites (Yuna, 2016), graphene-based nanomaterials (Ahmad et al., 2020), metal/covalent organic frameworks (Cao et al., 2021), and mesoporous carbons and carbon nanotubes (Fiyadh et al., 2019).

Most common adsorbents have low adsorption capacities and low separation rates; hence, it is essential to synthesize adsorbents with a high adsorption capacity. Magnetic nanoparticles, especially Fe_3O_4, have been widely used as the core materials in core-shell adsorbents due to their outstanding properties such as effective magnetic separation by an external magnetic field, low toxicity, biocompatible, easy and economic synthesis processes, and simple surface modification (due to the abundant hydroxyls on the surface of iron oxide) (Nowicka et al., 2019). However, magnetic nanoparticles tend to aggregate easily, something which could lead to surface area limitation and toilsome recycling (Vickers, 2017).

As a result, support materials should be introduced to ensure the homogeneous distribution of Fe_3O_4 nanoparticles for the adsorption process. Reportedly, the formation of a passive coating for magnetic nanoparticles can prevent their magnetic aggregations in the reaction mixture, thereby improving their chemical stability (Izgi et al., 2020). Most recently, magnetic nanocomposites with Fe_3O_4 cores and diverse organic and inorganic compounds as shells have been synthesized and used successfully as adsorbents to remove contaminants and perform water treatment (Narayan et al., 2018). For instance, humic acid-coated Fe_3O_4 nanoparticles were reported to be efficient in removing Hg(II), Pb(II), and Eu(III) (Yang et al., 2012).

Moreover, Abd Ali et al. described a novel chrysin-functionalized Fe_3O_4 core for the removal of Cu(II) from aqueous solutions, reporting an adsorption capacity of 114 mg g^{-1} (Abd Ali et al., 2016).

Silica can be an appropriate coating material to use as a protective layer due to its high specific surface area, low toxicity, favorable biocompatibility, low cost, and high availability that can remain stable under acidic conditions, helping to protect the inner magnetite Fe_3O_4 core. Not only does silica coating help magnetic nanoparticles' stability at certain conditions, but it is also easily modified with various silane coupling agents or compounds for adsorption (Salman et al., 2021). In many recent studies, some special groups and compounds have further branched on the silicon shell of core-shell absorbents to increase the activity and the adsorption site of absorbents.

Zhang et al. prepared five kinds of amino-functionalized magnetic Fe_3O_4/SiO_2 submicron composites (Zhang et al., 2014). Zhao et al. prepared 3-aminopropyltriethoxysilane (APTES) functionalized magnetic core-shell structure materials (Zhao et al., 2015). Amino functionalization has also been reported by other researchers (Reddy et al., 2014).

Bao et al. published the synthesis and analysis of mercapto amine-functionalized silica-coated magnetite for the removal of toxic metals such as Pb(II) with a maximum adsorption capacity of 292 mg g^{-1} (Bao et al., 2017).

There is an ever-increasing demand for silica nanospheres with different dimensions, surface areas, pore sizes, and morphologies for industrial applications. The absence of pores and insufficient surface areas of silica nanospheres would limit their applications in various fields. However, these issues were resolved with the discovery of mesoporous silica, which is synthesized

through templates to create pores and a large number of surfaces. Mesoporous silica materials—viz. hollow spheres, KIT-5, KIT-6, MCM-41, MCM-48, SBA-15, and SBA-16—have grown in popularity in the adsorption technology of numerous pollutants due to their unique properties such as large identical pore networks, high surface areas, functional surfaces, nontoxic nature of silica networks, availability of the synthetic raw materials, relatively low prices, and simple design of pore structures, and morphology (Soltani et al., 2020).

However, narrow pore sizes and the possibility of their blocking have limited the use of mesopores, especially for adsorption and separation (Sun et al., 2016). Mesoporous silica materials have now been developed and successfully utilized to remove heavy metal ions from aqueous media (Li et al., 2011a, Anbia et al., 2015, Vojoudi et al., 2017, He et al., 2021, Wang et al., 2020b, Hassan et al., 2022, Wang et al., 2020a).

A novel member of the MSMs[1] family is fibrous silica KCC^{-1}, which was first synthesized and characterized by Polshettiwar et al. (Polshettiwar et al., 2010). Polshettiwar reported that the large surface area of the material was caused by the presence of dendrimeric fibrous silica and their associated channels, which in turn made KCC^{-1} the first of its kind. In fact, KCC^{-1} has special center-radial pore structures with the pore sizes gradually increasing from the center to the surface. Conventional mesoporous silica materials (e.g., MCM-48, MCM-41, SBA-15, and SBA-16) have a narrow pore size distribution; however, KCC^{-1} possesses the channels that have divergently grown from the center. Variations in the sizes of these channels are proportionate to their distance from the center. Due to their radial-like direct channels and large pores, fibrous structured silica nanospheres (KCC^{-1}) help target molecules reach the active sites more easily than other mesoporous materials (Hasan and Setiabudi, 2019).

Hence, unlike traditional MSM materials with ordered channel-like pores, which are prone to pore-blocking phenomena leading essentially to the inaccessibility of several adsorption sites inside pores and channels, KCC^{-1} possesses a nanoporous fibrous architecture that dramatically enhances the accessibility to pores and available surface areas (Hasan et al., 2019).

Thus, KCC^{-1} performs better than the other silica mesoporous in adsorption-related applications (Singh and Polshettiwar, 2016). Hence, this study is primarily devoted to the synthesis of $Fe_3O_4/SiO_2/KCC^{-1}$ as a magnetic fibrous mesoporous adsorbent in Pb(II) ions adsorption process. The adsorption of Pb(II) onto the sorbent was analyzed with designed experiments through the CCD[2] under the RSM[3]. Analyses of adsorption isotherms, kinetics, thermodynamics, and desorption have also been conducted.

2.1. Materials and Equipments

All reagents used in the experiment were of analytical grade and did not require further purification. The reagents including TEOS[4] (98%), CTAB[5] (99%), $Pb(NO_3)_2$, NaOH and HCl were purchased from Merck Chemical Company (Germany). Cyclohexane, Pentanol, Urea, NH_4OH (25%), $FeCl_2.4H_2O$, $FeCl_3.6H_2O$, C_2H_5OH (99.8%) were purchased from Sigma-Aldrich Chemical Company. Deionized water was used to prepare all solutions.

A Scanning electron microscope (Hitachi SEM[6] 1460, Japan) at 20 kV was applied to determine the shape and structure of the particles. Transmission electron microscopy images were recorded on H-9500 (Phenomenex TEM[7] , US) electron microscope. For sample preparation, the sample was dispersed in ethanol with the assistance of sonication, and a drop of colloidal solution was placed on a carbon-coated TEM grid of 200 mesh and the solvent was evaporated in the air at room temperature. Then, the sample was transferred to an electron microscope operating at an accelerating voltage of 200 kV (Venkateswarlu et al., 2019).

The FTIR[8] (Perkin Elmer FTIR spectrophotometer) spectra were detected on a Nicolet Nexus 670 FTIR spectrometer using KBr pellets of the solid samples and the wavenumber range of the spectra were obtained from 400 to 4000 cm^{-1} with a 2 cm^{-1} resolution. The XRD[9] test was achieved via XRD instruments (Bruker AXS D8-advance diffractometer using CuKα radiation).

The scan range was 2θ=10-90° and λ=1.541874 A° at room temperature. Isotherms of N_2 adsorption and desorption were evaluated through a PHS-1020 apparatus at 77 K. The specific surface area was assessed using BET[10] theory, while pore volume was calculated through the BJH[11] technique. The magnetization assessment was obtained utilizing a SQUID magnetic susceptometer (VSM[12] , USA) at room temperature in an applied magnetic field sweeping from -15 to 15 kOe. Atomic-absorption instrument (Shimadzu, AA-670G) was employed to measure Pb(II) content in the solution. Statistical software "Design Expert" (version 12.0) was used for designing the experiments and analyses of the obtained data.

[1] Mesoporous Silica Materials (MSMs)
[2] Central Composite Design (CCD)
[3] Response Surface Methodology (RSM)
[4] Tetraethyl Orthosilicate (TEOS)
[5] Cetyltrimethylammonium Bromide (CTAB)
[6] Scanning Electron Microscope (SEM)
[7] Transmission Electron Microscopy (TEM)
[8] Fourier Transform Infrared (FTIR)
[9] X-Ray Powder Diffraction (XRD)
[10] Brunauer-Emmett-Teller (BET)
[11] Barrett-Joyner-Halenda (BJH)
[12] Vibrating Sample Magnetometer (VSM)

2.2. Adsorbent preparation

2.2.1. Preparation of Fe_3O_4/SiO_2 core-shell nanocomposite

The magnetic Fe_3O_4 nanoparticles were prepared by the chemical coprecipitation method (Jin et al., 2017). The synthesis of these particles was in order to form a silica coating on a magnetic core. The typical procedure is as follows:

Firstly, $FeCl_3 \cdot 6H_2O$ and $FeCl_2 \cdot 4H_2O$ with a molar ratio of 1:2 were dissolved into 100 mL of deionized water at 90 °C temperature and under nitrogen gas protection. Then, the $NH_3 \cdot H_2O$ (25% w/w, 100 mL) solution as the precipitant agent was added dropwise at the constant rate to the above solution under high-speed stirring (1000 rpm) for 20 min to reach a pH 10 value. As the concentration of ammonia increased, the color of the solution turned darker and eventually became black. The suspension was continuously stirred under a nitrogen atmosphere at 90 °C for 20 min and then cooled to room temperature.

The mixture was finally centrifuged, and black precipitates were washed three times with deionized water and ethanol and subsequently dried in a vacuum at 50 °C for 24 h. Nanoparticle size depends on the Ratio of Fe^{2+} and Fe^{3+}, pH value, and the temperature of the solution. The chemical coprecipitation can be expressed as follows (Eq. 1)

$$Fe^{2+} + 2Fe^{3+} + 8OH^- \rightarrow Fe_3O_4 + 4H_2O \quad (1)$$

In the next step, the Fe_3O_4/SiO_2 core-shell nanoparticles were produced with the Fe_3O_4 nanoparticles coating using a layer of silica following Stöber method and sol-gel process (Li et al., 2011b). The Fe_3O_4 nanoparticles were covered with silica particles to allow for further growth of fibrous silica (KCC^{-1}). In a typical run, the aforementioned prepared Fe_3O_4 nanoparticles (1.00 g) were treated with HCl aqueous solution (1 M) by sonication for 15 min. Then, the magnetic nanoparticles were separated and washed several times with deionized water. Thereafter, washed nanoparticles were homogeneously dispersed by ultrasonic treatments in a mixed solvent of anhydrous ethanol (80 mL) and deionized water (20 mL). Then, ammonia aqueous solution (2.5 mL, 25 wt%) was added to the solution. Subsequently, TEOS (2 mL) was added to the reaction mixture dropwise and it was then continuously stirred under mechanical stirring (600 rpm) for 12 h at room temperature. During this procedure, the TEOS hydrolyzed to form the silica oligomers, which cover the Fe_3O_4 nanoparticles.

The thus-formed Fe_3O_4/SiO_2 composites were centrifuged, washed several times with an ethanol-water mixture and finally dried under a vacuum at 50 °C for 12 h (Ding et al., 2012).

2.2.2. Preparation of the $Fe_3O_4/SiO_2/KCC^{-1}$ core–shell microspheres

The $Fe_3O_4/SiO_2/KCC^{-1}$ core-shell microspheres were synthesized according to the procedure described by Alamri et al. (Alamri et al., 2018). In this synthesis process, TEOS, CTAB, n-pentanol, cyclohexane, and urea were used as silica source, structure-directing agent (template), co-surfactant (for stabilizing the micelles/microemulsion droplets), co-solvent, and hydrolyzing agent, respectively. Briefly, the above-obtained Fe_3O_4/SiO_2) 3.00 g (powder was ultrasonically dispersed into an aqueous solution (100 mL) including CTAB (2.00 g) and urea (0.60 g). The resulting mixture was stirred for about 3 h at room temperature by vigorous stirring at 1200 rpm. The suspension was added to the solution containing n-pentanol (0.75 mL) and cyclohexane (30 mL) under stirring (600 rpm) at room temperature. To the above mixture, a solution of TEOS (1.25 g) was added dropwise over 20 min under stirring by using a dropping funnel and then stirred at 600 rpm at room temperature for 1 h. To continue, the mixture was refluxed at 120 °C for 24 h. Afterward, the solution was allowed to cool to room temperature and the obtained product was isolated by filtration, washed several times with deionized water and ethanol, and dried overnight in an oven at 40 °C. Finally, the dried precipitant was calcined at 550 °C for 5 h to remove the CTAB as a templating agent.

2.3. Experimental design

Response surface methodology includes different designs. In current study, a five-level central composite design was applied to evaluate the effects of four of the independent variables (pH, adsorption dosage, contact time, temperature) on the removal percentage of Pb(II) by $Fe_3O_4/SiO_2/KCC^{-1}$ adsorbent. Four independent process variables were converted as dimensionless (A, B, C, D), respectively. Five levels (-2(-α), -1, 0, 1, and +2(+α)) were used in order to design experiments as shown in Table 1.

2.3.1. Modeling and predicting the response

In this study, predicted responses by the CCD experimental design were better fitted with a second-order polynomial regression model which is called the quadratic model. Based on the proposed model, the correlation between the dependent variable and independent input variables and finally predicting the optimal response can be expressed by the following Equation (Eq. 2)

$$Y = \beta_o + \sum_{i=1}^{n} \beta_i X_i + \sum_{i=1}^{n} \beta_{ii} X_i^2 + \sum_{i=1}^{n-1} \sum_{j=i+1}^{n} \beta_{ij} X_i X_j + \varepsilon \quad (2)$$

 dx.doi.org/10.22093/wwj.2022.379990.3314

Table 1. Independent variables and their encoded levels

Symbol	Independent variables	Factor level				
		-2(-α)	-1(Low)	0(Center)	+1 (High)	+2(+α)
A	pH	4	5	6	7	8
B	Absorbent dosage	10	20	30	40	50
C	Contact time	20	30	40	50	60
D	Temperature	10	40	70	100	130

Where
Y represents the predicted response of the system, X_i, X_j are the independent variables, n is the total number of studied independent variables, β_o is the regression coefficient for the intercept (the interception coefficient), β_i , β_{ii}, β_{ij} are the coefficient values for linear, quadratic, and linear-linear interaction effects between X_i and X_j , respectively, and ε is the fitting error.

The obtained results were then analyzed using ANOVA[1] (Janighorban et al., 2020).

2.4. Batch adsorption studies

Batch adsorption experiments were carried out to study the adsorption behavior of Pb(II) ions onto the $Fe_3O_4/SiO_2/KCC^{-1}$. For each experiment, a certain amount of adsorbent 1 was added to 20 mL of standard solutions prepared from Pb(II). The solutions were then stirred for 12 h at room temperature. It was previously checked that this period of time (12 h) was enough to reach equilibrium adsorption. Finally, the suspensions were centrifuged for 5 min at 3000 rpm, and the residual Pb(II) concentrations in the solutions were measured employing an atomic absorption spectrophotometer. The initial pH of Pb(II) solution was adjusted using sodium hydroxide or hydrochloric acid solution. The removal percentage of the Pb(II) from aqueous (R%) and the adsorption capacities of the adsorbent for Pb(II) (q_t, mg g^{-1}) at anytime t were determined using the following equations (Eqs. 3 and 4):

$$R = \frac{C_0 - C_t}{C_0} \times 100 \quad (3)$$

$$q_{t=(C_0 - C_t)} \frac{V}{m} \quad (4)$$

Where
C_o (mg L^{-1}), Ct (mg L^{-1}), m (g L^{-1}), and V(mL) represent the initial concentration of Pb(II), the concentration of Pb(II) at any time (t), the mass of the adsorbent, and the volume of Pb(II) solution, respectively (Bayuo et al., 2020).

The optimal adsorbent dose (m= 0.04 g L^{-1}), pH (pH=5.6), and T (80 °C) values were selected according to the optimization experiments in the current study and were kept constant throughout the adsorption experiments. The statistical parameter R^2, the coefficient of determination, was used to decide which isotherm or kinetic model is more consistent with the experimental data after the linear fitting method.

3. Results and discussion

3.1. Adsorbent characterization

The SEM technique was employed to analyze the shape and surface morphology of the Fe_3O_4/SiO_2 and $Fe_3O_4/SiO_2/KCC^{-1}$ samples. In the preparation of $Fe_3O_4/SiO_2/KCC^{-1}$, Fe_3O_4 NPs were covered by amorphous silica to form Fe_3O_4/SiO_2 in order to allow for the further growth of fibrous nano-silica (KCC^{-1}).

According to Figs. 1a and 1b, morphology of Fe_3O_4/SiO_2 particles changed considerably after they were coated with KCC^{-1}, something which confirmed the presence of KCC^{-1} attached to the surface of the Fe_3O_4/SiO_2. Both synthesized composites (Fe_3O_4/SiO_2 and $Fe_3O_4/SiO_2/KCC^{-1}$) were spherical; however, they were characterized by distinguished morphological differences. According to Fig. 1a, the nanospheres Fe_3O_4/SiO_2 surface was slightly rough and had no fiber structures. The SEM images of $Fe_3O_4/SiO_2/KCC^{-1}$ demonstrated that it had fibrous and wrinkled morphology, clearly visible pore channels, and acceptable dispersity. Therefore, $Fe_3O_4/SiO_2/KCC^{-1}$ is mainly composed of monodisperse spherical particles with fibrous morphology. In fact, these particles are non-aggregated with narrow distribution indicating the expected high porosity and large specific $Fe_3O_4/SiO_2/KCC^{-1}$ surface area . The close inspection of $Fe_3O_4/SiO_2/KCC^{-1}$ by the TEM technique (Fig. 2) indicated that those samples had dendrimer fibers arranged within a 3D space to form uniform spheres. The TEM images revealed the porous, fibrous, and dendritic structures of $Fe_3O_4/SiO_2/KCC^{-1}$ magnetic composites. Moreover, the dimensions of $Fe_3O_4/SiO_2/KCC^{-1}$ MNPs were evaluated through the TEM. The $Fe_3O_4/SiO_2/KCC^{-1}$ MNPs were approximately 98 nm long, and the distance between the two fibers was nearly 28.5 nm. The larger the distance between the fibers, the easier the loading of the Pb(II) on $Fe_3O_4/SiO_2/KCC^{-1}$. The highly-ordered tunnels and high surface areas in this adsorbent accelerated the adsorption process.

The FTIR spectrum helps identify the nanomaterials through the analysis of functional groups. Fig. 3 demonstrates the FTIR spectra of the $Fe_3O_4/SiO_2/KCC^{-1}$.

[1] Analysis of Variance (ANOVA)

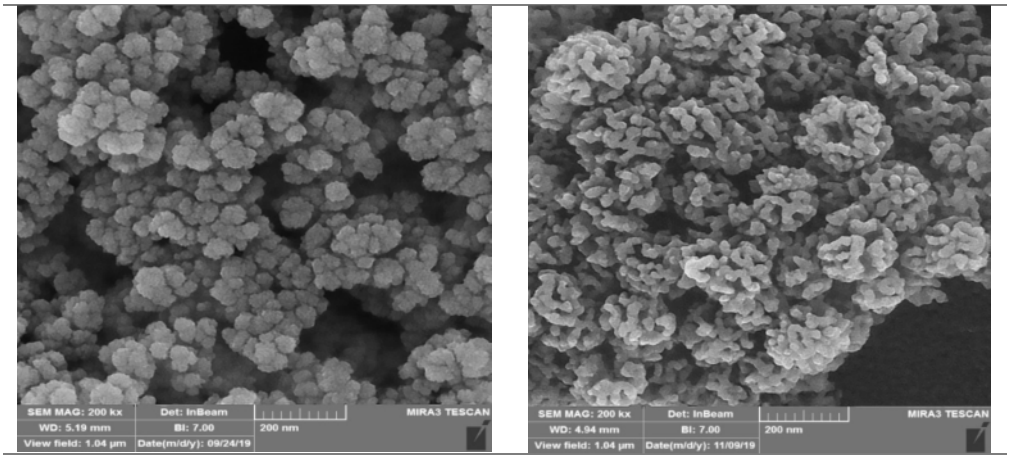

a b

Fig. 1. a) The SEM image of Fe_3O_4/SiO_2 and b) the SEM image of $Fe_3O_4/SiO_2/KCC^{-1}$

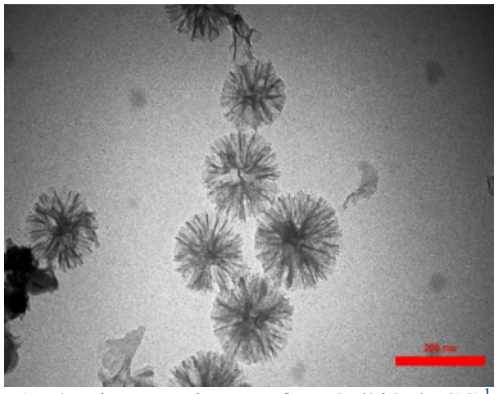

Fig. 2. The TEM image of $Fe_3O_4/SiO_2/KCC^{-1}$

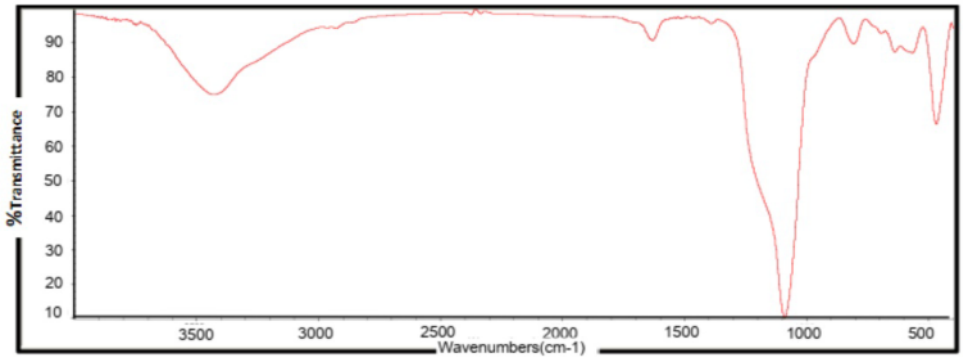

Fig. 3. The FTIR spectra of $Fe_3O_4/SiO_2/KCC^{-1}$

The absorption bands at about 460 cm^{-1}, 1080 cm^{-1}, and 801cm^{-1} are attributed to the asymmetric Si-OH stretching vibration, Si-O stretching vibration, and Si-O-Si bending vibration modes, respectively (Yu et al., 2013).

These observations are in close agreement with previous results regarding mesoporous silica materials (Soltani et al., 2018, Soltani et al., 2019b, Soltani et al., 2019a). Similarly, a broad band at 3428 cm^{-1} and a peak at 1630 cm^{-1} correspond to the Si-OH stretching and water molecules absorbed on the KCC^{-1} surface, respectively.

The presence of silanol groups in KCC^{-1} is beneficial to the adsorption process as the presence of negative charge results in a larger number of available active sites for the adsorption process. Moreover, the peak at 560 cm^{-1} is characterized by Fe–O stretching vibrations (Yu et al., 2013). These results successfully confirm the presence of all three components, including KCC^{-1}, SiO_2, and Fe_3O_4, in the adsorbent structure (Yu et al., 2013).

 dx.doi.org/10.22093/wwj.2022.379990.3314

Fig. 4 illustrates the N_2 adsorption–desorption isotherm of $Fe_3O_4/SiO_2/KCC^{-1}$. According to the IUPAC classification, a type-IV isotherm with an evident H1-type hysteresis loop was exhibited. It revealed strong evidence for mesoporous cylindrical or rod-like pores. The surface area, pore volume, and pore size of synthesized $Fe_3O_4/SiO_2/KCC^{-1}$ were reported 813.07 $m^2 g^{-1}$, 1.41 $cm^3 g^{-1}$, and 7.94 nm, respectively. The high surface area of $Fe_3O_4/SiO_2/KCC^{-1}$ will improve the accessibility of Pb(II) molecules to the $Fe_3O_4/SiO_2/KCC^{-1}$, thereby enhancing the adsorption process. Moreover, the outcomes from N_2 adsorption/desorption analysis indicated that the proposed method for removing the template from the structure was very successful. This method also withdrew nearly all the surfactant and produced an effective adsorbent with higher surface areas than those of the same structures reported by previous studies (Table 2).

The crystalline structure of the magnetic nanocomposite was determined through X-ray diffraction. Fig. 5 demonstrates the X-ray diffraction patterns of $Fe_3O_4/SiO_2/KCC^{-1}$. The four diffraction peaks located at $2\theta = 30.30, 35.60, 43.20$, and 57.20 corresponding to the (220), (311), (400), (511), and (440) crystal planes, respectively, indicate the characteristic peaks of Fe_3O_4 NPs (JCPDS NO. 19-0629), which confirmed that the Fe_3O_4 nanoparticles embedded in the core had not changed despite being calcined at 550 °C. Furthermore, the wide peak within the range of 2θ from 15 to 30° was a characteristic of the amorphous siliceous phase in KCC^{-1}. The sharp and strong peaks confirmed that the product was crystallized properly. The magnetic properties of the nanospheres were characterized through a vibrating sample magnetometer at room temperature. In the $Fe_3O_4/SiO_2/KCC^{-1}$ nanospheres, the Fe_3O_4 core is responsible for magnetic removal. The magnetization curves of the synthesized adsorbent indicated no hysteresis loops (Fig. 6), a finding which means that the nanocomposite exhibited paramagnetic characteristics.

The measured saturation magnetization (Ms) value was 62.8 emu g^{-1}. Having paramagnetic characteristics and high magnetization values, these nanocomposites can quickly respond to the external magnetic field and quickly re-disperse when the external magnetic field is removed.

3.2. Central composite design

The maximum Pb(II) removal efficiency and the impacts of the studied independent parameters on the Pb(II) adsorption were analyzed through the experiments

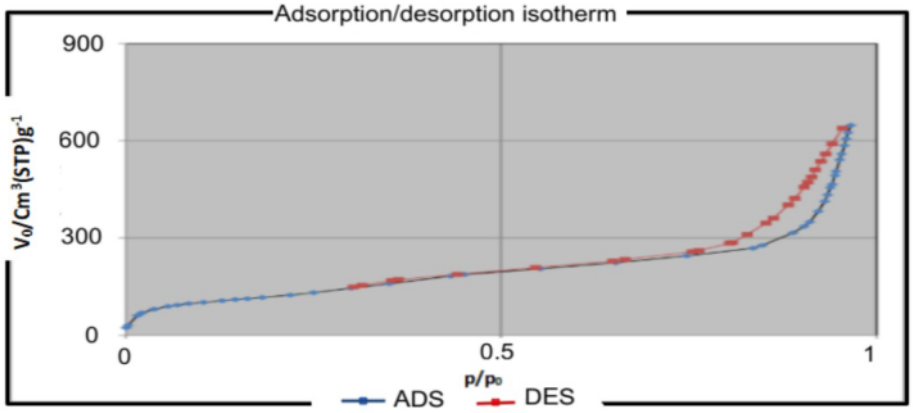

Fig .4. The N_2 adsorption and desorption isotherm of $Fe_3O_4/SiO_2/KCC^{-1}$

Table 2. Comparison of some reported surface areas for magnetic mesoporous materials in the research literature

BET surface area ($m^2 g^{-1}$)	Reference
382	(Lapwanit et al., 2016)
316	(Hao et al., 2010)
705	(Monier et al., 2010)
86.10	(Xu et al., 2010)
820	(Xu et al., 2006)
172	(Wang et al., 2011)
593	(Abdollahi et al., 2012)
17.31	(Zhao et al., 2013)
813.07	This work

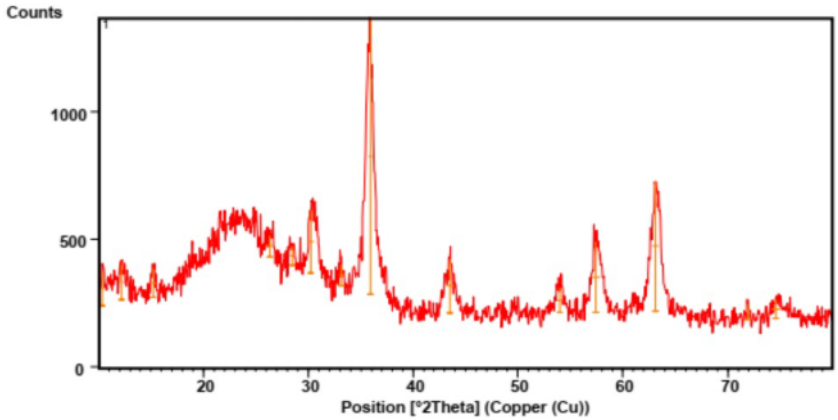

Fig .5. XRD patterns of $Fe_3O_4/SiO_2/KCC^{-1}$

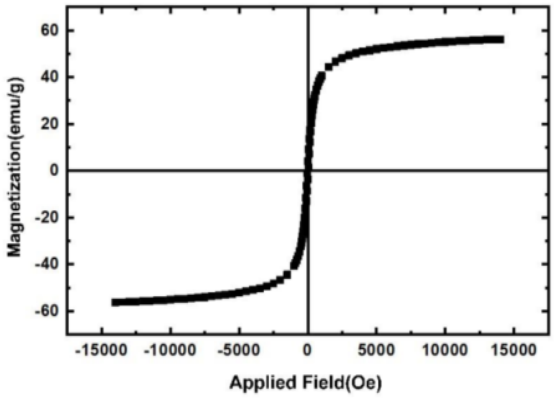

Fig. 6. The VSM magnetization curve of $Fe_3O_4/SiO_2/KCC^{-1}$

designed in the CCD-based RSM. For this purpose, 30 experiments including 16 factorial points, 8 axial points (α=±2), and 6 repeats of center points were designed in the stipulated conditions based on the CCD to optimize the studied variables. The experiments were conducted in this software design. Table 3 reports the results of the dependent variable in each run (experimental responses). The total number of experimental runs by a central composite design is computed through Eq. 5

$$N = 2^k + 2k + n \quad (5)$$

Where
k denotes the number of independent variables, and N represents the overall number of experimental runs. In the above equation, 2^k refers to fractional factorial design points consisting of possible combinations of high (+1) and low (-1) levels of each factor, which reflect the main effects and the interactions between parameters. Furthermore, $2k$ indicates the axial points which were fixed axially at a distance (α) from the center to generate quadratic terms. In other words, if the distance from the center of the design space to a factorial point is ±1 coded unit for each factor, the distance from the center of the design space to an axial point will be |α|>1. The axial points are obtained from the experiments outside the intended range for each factor. The value of α depends on the type of the offered CCD and the number of independent variables. Moreover, n is the center point which represents replicate terms. Center points come from the experiments that run at the center level of each factor range and provide a good estimate of the experimental error. They may vary from three to six (Moosazade et al., 2021).

3.3. Model fitness and statistical analysis

In order to analyze the significance and suitability of the regression model obtained from the RSM, an analysis of variance was conducted to examine the experimental responses. Table 4 reports the results. The significance of the regression model and its terms were determined by F and P values through Fisher's test and a null hypothesis (Rahimi et al., 2021). The F-value is the mean square regression (2385.93019) divided by the mean square residual (51.0963039). In this study, the critical F-value at a 99% confidence level was much smaller than the experimental F-value, a finding which confirmed that the proposed model was significant and

 dx.doi.org/10.22093/wwj.2022.379990.3314

Table 3. The matrix design and responses

Run No.		Variables								Response	
		Factor1 A: pH		Factor2 B: Absorbent dose (mg L^{-1})		Factor3 C: Contact time(min)		Factor4 D: Temperature(^{o}C)		Removal%	
		Actual	Coded	Actual	Coded	Actual	Coded	Actual	Coded	Actual	Predicted
1	Axial	6	0.000	10	-2.000	40	0.000	70	0.000		86.45
2	Axial	6	0.000	30	0.000	60	2.000	70	0.000		89.15
3	Center	6	0.000	30	0.000	40	0.000	70	0.000		92.25
4	Factorial	7	1.000	20	-1.000	30	-1.000	40	-1.000		82.87
5	Factorial	7	1.000	40	1.000	50	1.000	40	-1.000		82.91
6	Axial	6	0.000	50	2.000	40	0.000	70	0.000		91.8
7	Factorial	7	1.000	20	-1.000	50	1.000	100	1.000		83.73
8	Axial	6	0.000	30	0.000	40	0.000	130	2.000		93.64
9	Factorial	7	1.000	20	-1.000	30	-1.000	100	1.000		85.63
10	Axial	6	0.000	30	0.000	40	0.000	10	-2.000		85.7
11	Axial	6	0.000	30	0.000	20	-2.000	70	0.000		92.6
12	Factorial	5	-1.000	20	-1.000	30	-1.000	40	-1.000		86.83
13	Factorial	7	1.000	40	1.000	30	-1.000	40	-1.000		85.91
14	Factorial	7	1.000	40	1.000	30	-1.000	100	1.000		89.33
15	Center	6	0.000	30	0.000	40	0.000	70	0.000		92.13
16	Center	6	0.000	30	0.000	40	0.000	70	0.000		92.2
17	Axial	8	2.000	30	0.000	40	0.000	70	0.000		73.8
18	Factorial	5	-1.000	40	1.000	50	1.000	100	1.000		92.63
19	Factorial	7	1.000	40	1.000	50	1.000	100	1.000		86.88
20	Factorial	5	-1.000	20	-1.000	50	1.000	100	1.000		90.29
21	Factorial	5	-1.000	20	-1.000	30	-1.000	100	1.000		90.98
22	Factorial	5	-1.000	40	1.000	30	-1.000	40	-1.000		88.98
23	Factorial	5	-1.000	20	-1.000	50	1.000	40	-1.000		85.74
24	Center	6	0.000	30	0.000	40	0.000	70	0.000		92.15
25	Center	6	0.000	30	0.000	40	0.000	70	0.000		92.2
26	Factorial	5	-1.000	40	1.000	30	-1.000	100	1.000		93.75
27	Factorial	5	-1.000	40	1.000	50	1.000	40	-1.000		87.6
28	Center	6	0.000	30	0.000	40	0.000	70	0.000		92.28
29	Axial	4	-2.000	30	0.000	40	0.000	70	0.000		83.72
30	Factorial	7	1.000	20	-1.000	50	1.000	40	-1.000		80.31

Table 4. ANOVA of dependent variable based on the response surface quadratic model

Source of variation	df	Sum of Squares(SS)	Mean Squares(MS)	F-value	P-value	
Regression	14	620.43	44.32	10456.03	< 0.0001	Significant
Residual	15	0.0636	0.0042			
Lack of fit	10	0.0473	0.0047	1.45	0.3567	Not significant
Pure error	5	0.0163	0.0033			

Table 5. ANOVA of the quadratic model for removal of Pb(II)

Variables	df	Sum of Squares(SS)	Mean Squares(MS)	F-value	P-value	
A-pH	1	145.39	145.39	34302.64	< 0.0001	Significant
B- Adsorbent dosage	1	43.50	43.50	10262.84	< 0.0001	Significant
C-Contact time	1	18.53	18.53	4372.64	< 0.0001	Significant
D-Temperature	1	95.80	95.80	22603.25	< 0.0001	Significant
AB	1	0.7098	0.7098	167.47	< 0.0001	significant
AC	1	1.98	1.98	467.41	< 0.0001	Significant
AD	1	1.52	1.52	358.41	< 0.0001	Significant
BC	1	0.1828	0.1828	43.12	< 0.0001	Significant
BD	1	0.3335	0.3335	78.69	< 0.0001	Significant
CD	1	0.2186	0.2186	51.57	< 0.0001	Significant
A2	1	308.49	308.49	72785.10	< 0.0001	Significant
B2	1	15.94	15.94	3761.57	< 0.0001	Significant
C2	1	2.90	2.90	683.12	< 0.0001	Significant
D2	1	10.75	10.75	2537.23	< 0.0001	Significant

df: degree of freedom of source of variance; SS: sum of square; MS: mean square (the ratio of sum of square to degree of freedom of each term); P-value: probability of error to be significant; F: MS/MS residua.

could properly process the experimental data. In addition, if the p-value for the F-test is smaller than the significance level, it indicates that the model fits properly with the experimental data (Dahlan et al., 2022).

According to the ANOVA of the quadratic regression model, the proposed model from the RSM with "Prob>F" less than 0.01 was statistically significant. Hence, there was only a 0.01% chance that the model could be affected by noise, and most of the variation in the response was explained by the regression equation. In fact, the ANOVA indicated a significant and accurate relationship between the response and independent variable. Moreover, a regression model exhibits lack of fit when it fails to adequately describe the functional relationship between the experimental factors and the response variable. In the RSM, if the p-value of LOF[1] is larger than the significance level α, it implies that the proposed model fits the experimental data (Bhattacharya, 2021).

According to Table 4, the LOF of the proposed regression model was non-significant. The F values can be employed to estimate the significant effect of each parameter on the response variable. The highest F value indicates more importance of a factor (Dan et al., 2021). All the linear, quadratic, and interactional effects on the response were significant ($p < 0.0001$) in this study (refer to Table 5). Among the terms including single terms, the sequence of pH > temperature>adsorption dosage > contact time with F values of 34302.64, 22603.25, 10262.84, and 4372.64, respectively, indicated the importance of their effects on the response.

Among the terms including interactional effects, the sequence of pH-contact time > pH-temperature>pH-adsorption dosage > adsorption dosage-temperature > adsorption dosage-contact time was observed to have the F values of 467.41, 358.41, 167.47, 78.69, and 43.12. Among the quadratic terms, pH^2, adsorption $dosage^2$, and $temperature^2$ with F values of 72785.10, 3761.57, and 2537.23, respectively, indicated the most important effect on the response variable Y.

The following second-order polynomial equation was expressed as the final regression model (Eq. 6)

$$R\%(Pb(II)) = 92 \cdot 20 - 2 \cdot 46A + 1 \cdot 35B - 0 \cdot 87C + 2 \cdot 00D + 0 \cdot 21AB - 0 \cdot 35AC - 0 \cdot 31AD - 011BC + 0 \cdot 14BD + 0 \cdot 12CD - 3 \cdot 35A^2 - 0 \cdot 76B^2 - 0 \cdot 32C^2 - 0 \cdot 63D^2 \quad (6)$$

Where
A = pH, B = adsorption dosage, C = contact time, D = temperature.

In Eq. (6), the positive sign suggests a synergistic effect, whereas the negative sign indicates antagonistic behaviour (Manzar et al., 2021). Accordingly, temperature and pH are the most important parameters that affect Pb(II) adsorption on $Fe_3O_4/SiO_2/KCC^{-1}$. Furthermore, at a higher temperature and a lower pH, a higher removal efficiency could be achieved.

3.4. Interactions of variables

The combined effects of two factors on the predicted response were visualized by the 3D surface plots (Fig. 7). These plots are employed to evaluate the behavior of the whole adsorption system. In fact, they show how parameters affect the response (Torğut et al., 2020). The surface plots were generated from the model by varying any two variables within the limit of the experimental range while keeping the other independent factors

[1] Lack of Fit (LOF)

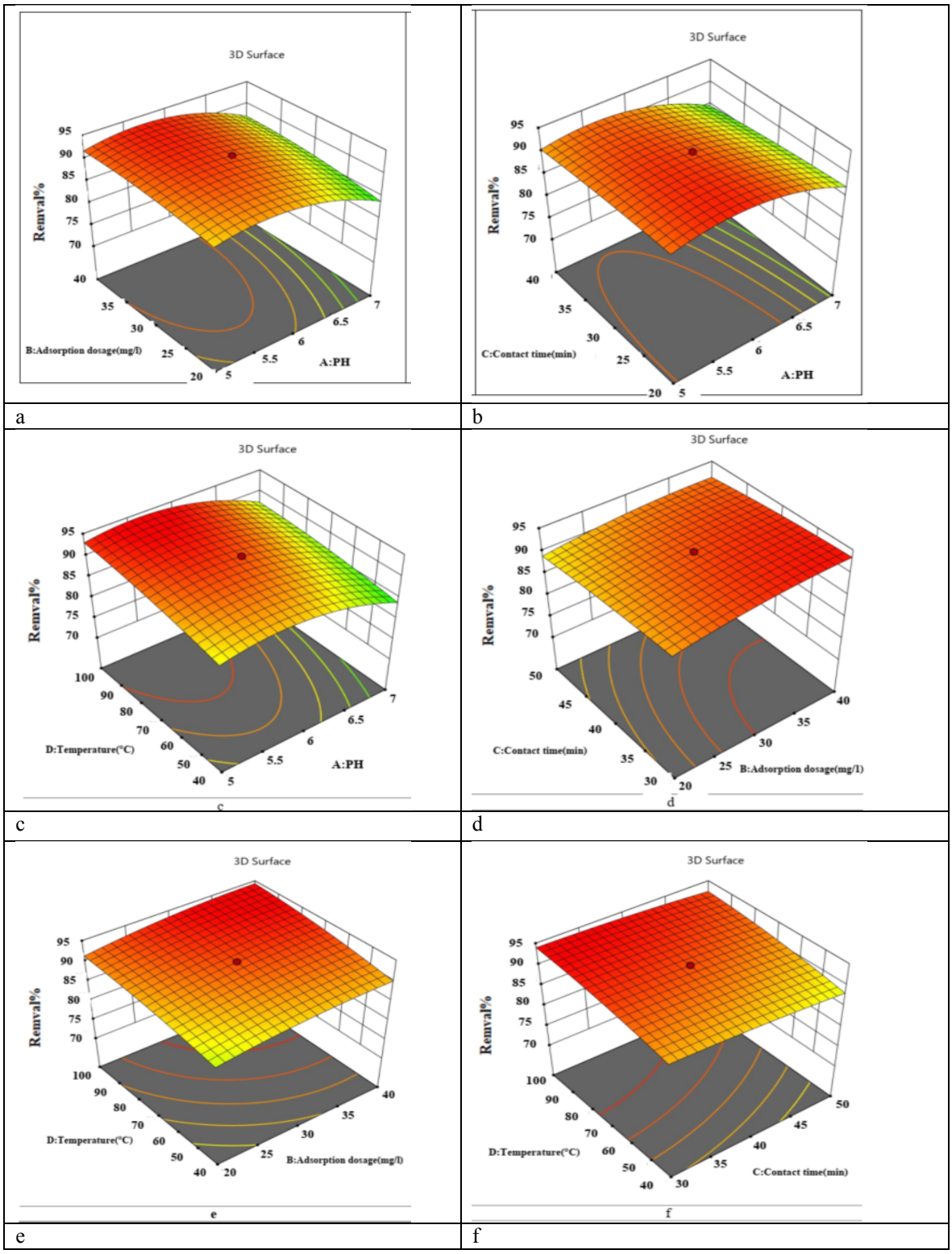

Fig. 7. Response surface plots for the efficiency of Pb(II) removal as a function of two independent variables: a) absorbent dosage and pH, b) contact time and pH, c) temperature and pH, d) contact time and absorbent dosage, e) temperature and absorbent dosage and f) temperature and contact time

constant at their midpoint (null point). The pH of the solution is a very crucial parameter in the adsorption process. According to Figs. 7a, 7b, and 7c, as the pH increased, the removal percentage increased up to a certain point and then decreased slightly. The maximum removal efficiency of Pb(II) was observed in nearly neutral conditions. By increasing pH, the removal of Pb(II) exhibited a downward trend. According to Figs. 7c, 7e, and 7f, the adsorption efficiency increased as the temperature increased. This trend can ensue from the activated sorption surface and the increased pore size; hence, the diffusion of Pb(II) ions into the $Fe_3O_4/SiO_2/KCC^{-1}$ pores escalated. Another probable reason for this upward trend is the increasing diffusion rate of the Pb(II) molecules from the solution to the liquid–solid interphase (Topal and Topal, 2020), as a result of a decrease in the viscosity of the solution.

According to the trends observed in Figs. 7a, 7d, and 7e, the removal percentage increased with an increase in the adsorbent dose. This increase can be attributed to the enhanced active sites while increasing the adsorbent dosage (Joshi et al., 2020). According to Figs. 7b, 7d, and 7f, the removal efficiency of the used nanocomposite adsorbent was affected by the contact time parameter due to the equilibrium nature of lead (II) removal, and the removal efficiency slowly increased as the contact time between lead ions and adsorbent increased.

3.5. Optimization of process parameters

Fig. 8 demonstrates the ramp function graph of maximum desirability value for the numerical optimization of five goals: adsorbent dosage, temperature, contact time, pH, and lead removal percentage. The optimization was performed at the initial concentration of 10 mg/L while the agitation speed was fixed at 180 rpm. The optimal conditions for the maximal removal percentage included a temperature of 80 $^{\circ}C$, an adsorption dosage of 0.04 g L^{-1}, a pH of 5.6, and a contact time of 38 min.

According to Table 6, a predicted removal efficiency of 93.97% was found by the model under these optimized operations. Furthermore, the removal efficiency was determined under these optimal conditions experimentally. The results indicated that the predicted response and the experimental response were in very good agreement (Table 6). The high degree of agreement between the predicted optimal conditions and the repeated experimental results signaled that the central composite design could be used as an effective and reliable tool to evaluate and optimize the effects of adsorption parameters on the efficiency of Pb(II) removal through the $Fe_3O_4/SiO_2/KCC^{-1}$ nanocomposite. The initial pH of heavy metal solutions is among the most important parameters affecting the adsorption efficiency. In fact, at low pH values, due to the presence of excessive amounts of H^+ ions in the solution, a competition occurs between Pb^{2+} and H^+ in active sites on the adsorbent surface at the repulsion of Pb^{2+} as well as the protonated adsorbent surface. Hence, the removal efficiency decreases (Khan et al., 2020).

Moreover, when the pH is very acidic, the structure of the adsorbent dissolves, and hydrolysis of the tissues will occur inside the structure. As a result, the removal efficiency is lower at these pH values. However, at high pH values, despite the increase in deprotonation of the adsorbent surface, Pb(II) ions tend to precipitate in the form of metal hydroxide (e.g., Pb $(OH)_2$), something which affects the absorption process, eventually reducing the removal efficiency (Cheraghipour and Pakshir, 2020).

Furthermore, the effects of the point of zero charge (pH_{pzc}) value of the adsorbent on the Pb(II) adsorption were analyzed. To interpret the effect of pH on the adsorption process, pH_{pzc} is considered an effective parameter. The pH_{pzc} value of $Fe_3O_4/SiO_2/KCC^{-1}$ was reported approximately 4.7, a finding which meant that the surface charge of $Fe_3O_4/SiO_2/KCC^{-1}$ adsorbent was positive at pHs below pH_{pzc}, whereas it changed from positive to negative as pHs exceeded pH_{pzc} (Khan et al., 2021).

Hence, the removal percentage of Pb(II) increased at pH values above pH_{pzc} due to the attractive interaction, whereas it decreased at pH values below pH_{pzc} because of the electrostatic repulsion. In conclusion, Pb(II) adsorption reached the maximum at an approximate pH of 5.6 in the end. According to the optimization results, the adsorption process with the mesoporous $Fe_3O_4/SiO_2/KCC^{-1}$ composites was endothermic, a finding which was also confirmed by the thermodynamic results. In other words, the attractive forces between metal ions and the adsorbent surface became stronger at higher temperatures, and then the adsorption capacity increased. The increase in the uptake of metal ions with temperature might be due to the dissolution of the sorbing species and changes in the sizes of the pores (Fattahi et al., 2021).

Moreover, Pongsumpun et al. reported that increasing adsorption with an increase in temperature indicated an increase in the mobility of the metal ions and a corresponding increase in the frequency of collision between the adsorbate and the adsorbent (Pongsumpun et al., 2020).

Dao et al. suggested that increasing temperature might cause a swelling effect within the internal structure of the adsorbent, enabling metal ions to penetrate further (Dao et al., 2020).

The results also showed that the adsorption of lead ions on $Fe_3O_4/SiO_2/KCC^{-1}$ adsorbent was fast, and the adsorption efficiency reached a maximum value within 38 min. The obtained short adsorption time might be due to the presence of abundant active sites on the surface of

 dx.doi.org/10.22093/wwj.2022.379990.3314

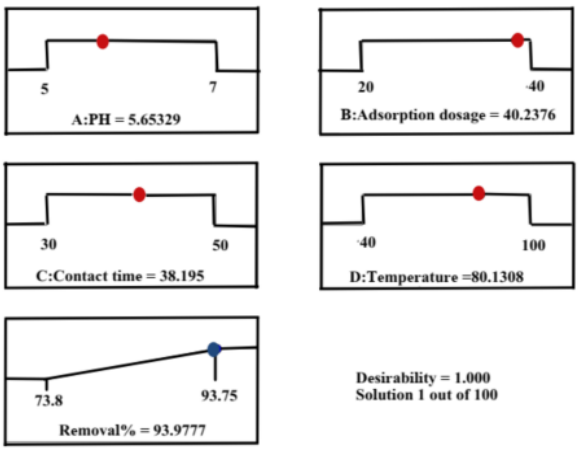

Fig .8. The ramp function graph of desirability

fibrous silica nanospheres. This feature can be attributed to the high surface area of adsorption. The amount of adsorbent is another important parameter that can determine the adsorption capacity for a given initial concentration. The conglomeration or overlapping of the active adsorption sites with an increase in the adsorption dosage would lead to a decrease in the absorption efficiency (Dehghani et al., 2020).

3.6. Analysis of adsorption isotherm

The relationship between the amount of a substance adsorbed per the unit mass of an adsorbent at constant temperature and its concentration in the equilibrium solution is known as the adsorption isotherm. For the solid-liquid system, adsorption isotherms must be analyzed to determine the adsorption capacity and the interaction between an adsorbate and an adsorbent (Razmi et al., 2019).

The linearized Langmuir and Freundlich isotherms models were used for the fitting of experimental data. For this purpose, several experiments with different initial concentrations (C_0= 0.5–250 mg L^{-1}) of Pb(II) were conducted under optimal conditions for 12 hours. Langmuir's adsorption model is based on the assumption that intermolecular forces decrease rapidly with distance and consequently predict the presence of a monolayer cover of the adsorbate on the outer surface of the adsorbent. This model also assumes that adsorption occurs in certain homogeneous regions within the adsorbent and that all adsorption zones are the same and energetically equivalent. Unlike the Langmuir isotherm, the Freundlich isotherm can be employed for multilayer adsorption on heterogeneous sites. According to the Freundlich isotherm, the adsorption heat distribution and affinities towards the heterogeneous surface are non-uniform. The values of the correlation coefficients (R^2) for the datasets were used as indicators of conformity between experimental data and the corresponding values predicted by each model. Basically, the closer the value of R^2 is to 1, the better the model fits the experimental data.

Table 7 presents the parameters calculated in the two isotherm models along with their correlation coefficients (R^2). According to Table 7, the adsorption of Pb(II) with $Fe_3O_4/SiO_2/KCC^{-1}$ can be best explained by Langmuir's model with a higher regression coefficient (R^2) as opposed to the Freundlich model. Therefore, Langmuir's model fitted the empirical data better. According to Table 7, the calculated maximum adsorption capacity (574.4) obtained by Langmuir's model was close to the corresponding experimental value (552.5), a finding which indicated the good agreement of this model with the experimental data. Hence, the agreement of Langmuir's model with the experimental results indicated that a monolayer of Pb(II) cations was adsorbed on the surface of $Fe_3O_4/SiO_2/KCC^{-1}$. In addition, the values obtained for 1/n within the range of $0 < 1/n < 1$ indicated that the adsorption was favorable; if $1/n > 1$, adsorption is unfavorable, and if $1/n = 1$, adsorption is irreversible (Eltaweil et al., 2020). According to Table 7, the value of 1/n for the adsorbent was below 1.0, something which reflected the desirability of the adsorption process.

In order to compare the adsorption efficiency of the present adsorbent with those of the adsorbents synthesized in previous studies, Table 8 presents the maximum adsorption capacities. Evidently, the $Fe_3O_4/SiO_2/KCC^{-1}$ adsorbent exhibited promising Pb(II) adsorption capacity compared with other adsorbents. Table 9 reports the constants of Langmuir's and Freundlich's models for the adsorption of Pb(II) onto some mesoporous adsorbents synthesized in previous studies. According to the coefficients of correlation obtained from linear regression, Langmuir's model fit the data better than Freundlich's model in all cases.

3.7. Analysis of adsorption kinetics

The adsorption kinetics were analyzed in order to better understand the dynamics of metal adsorption on the adsorbent and develop a predictive model to estimate the amount of adsorbed ions within the process. The rate of retention or release of a solute from an aqueous solution to the solid-phase interface can be described by adsorption kinetics in certain experimental conditions such as adsorbent dosage, flow rate, temperature, and pH (Xu et al., 2018).

Therefore, two common kinetic models called pseudo-first-order and pseudo-second-order models were employed to analyze the kinetic behavior of Pb(II) adsorption in $Fe_3O_4/SiO_2/KCC^{-1}$. The adsorption kinetics were analyzed by varying the time from 0 to 120 min at the room temperature with an initial concentration of 100 mg L^{-1} in optimal conditions. According to the PFO[1] and

[1] Pseudo-First-Order (PFO)

Table 6. The values of the optimized process variables for Pb(II) adsorption with the $Fe_3O_4/SiO_2/KCC^{-1}$ nanocomposite

Adsorbent dosage ($g\ L^{-1}$)	Temperature (°C)	pH	Contact time (min)	%Removal	
				Predicted	Experimental
0.04	80	5.6	38	93.97	90

Table 7. Isotherm constant parameters and correlation coefficients calculated for Pb(II) adsorption with the $Fe_3O_4/SiO_2/KCC^{-1}$ nanocomposite

Model	Equation	Parameters	Value	$q_{m,exp}$.($mg\ g^{-1}$)
Langmuir	$\frac{C_e}{q_e} = \frac{1}{K_L\ q_m} + \frac{C_e}{q_m}$	$q_{m,cal}$ ($mg\ g^{-1}$) K_L ($L\ mg^{-1}$) R^2	574.4 0.098 0.98	552.5
Freundlich	$\ln q_{e=} \ln K_f + \frac{1}{n}\ln C_e$	K_f ($mg\ g^{-1}$)($L\ mg^{-1}$)$^{1/n}$ n R^2	148.7 3.83 0.95	

Where $q_{m,cal}$ is the maximum adsorption capacity reflected a complete monolayer (mg/g), K_L is the Langmuir constant or adsorption equilibrium constant ($L\ mg^{-1}$), 1/n is the isotherm constant indicates the empirical parameter, K_F is the isotherm constant indicates the capacity parameter (mg/g) $(L/mg)^{1/n}$

Table 8. Comparison of the maximum adsorption capacity (q_{max}) of various mesoporous composite reported in the literature for removal of Pb(II)

Adsorbents	Maximum adsorption capacity (q_{max}, $mg\ g^{-1}$)	Reference
CMA	175.16	(Awual, 2019)
Commercial activated carbon (CGAC)	27.3	(Asuquo et al., 2017)
Ligand immobilized mesoporous	200.80	(Awual et al., 2014)
IIMS-MCM-41	344.8	(Cui et al., 2017)
Fe_3O_4@MCM-41-NH-oVan	155.71	(Cui et al., 2017)
NH_2-MCM-41	57.74	(Heidari et al., 2009)
NH_2-HMS	119.04	(Javadian et al., 2017)
Fe_3O_4@ MCM-41-NH_2	268.0	(Mehdinia et al., 2015)
EDTA-modified mesoporous silica SBA-15	273.2	(Huang et al., 2012)
Graphene/activated carbon (GAC)	217.6	(Saeidi et al., 2015)
AH-1	377.17	(Wu et al., 2012)
AF-Fe_3O_4	369.0	(Xin et al., 2012)
LMS-AP	48.7	(Li et al., 2018)
SBA-16-g	289.9	(Gupta et al., 2019)
$Fe_3O_4/SiO_2/KCC^{-1}$	574.4	This work

Table 9. Langmuir's and Freundlich's isotherm constants for the adsorption of Pb(II) onto various mesoporous adsorbents

Langmuir equation	Adsorbent	q_m (mg g^{-1})	K_L (L mg^{-1})	R^2	Reference
	SNF/MNP/PS	243.9	0.0542	0.990	(Li et al., 2018)
	NZVI-SH-HMS	580.0	0.0760	0.8924	(Li et al., 2021)
	Fe_3O_4@SiO_2-EDTA	101.01	0.40	0.9984	(Liu et al., 2016)
	Fe_3O_4@ MCM-41-NH_2	268	1.98	0.997	(Mehdinia et al., 2015)
	Fe_3O_4@SBA-15-NH_2-H	243.9	2.05	0.9997	(Wang et al., 2015)
	Fe_3O_4@SiO_2–NH_2	361.1	0.065	0.9945	(Zhang et al., 2013)
	PVP–SBA-15	175.439	0.0067	0.996	(Betiha et al., 2020)
	Pb-IIMS-SBA-15	211.4	2.3107	0.9932	(Cui et al., 2017)
	This work	574.4	0.098	0.98	-
Freundlich equation	**Adsorbent**	**K_f (mg g^{-1})(L mg^{-1})$^{1/n}$**	**n**	**R^2**	**Reference**
	SNF/MNP/PS	28.52	2.20	0.935	(Li et al., 2018)
	NZVI-SH-HMS	12.340	3.003	0.7995	(Li et al., 2021)
	Fe_3O_4@SiO_2-EDTA	49.71	6.79	0.5908	(Liu et al., 2016)
	Fe_3O_4@ MCM-41-NH_2	106.6	2.00	0.941	(Mehdinia et al., 2015)
	Fe_3O_4@SBA-15-NH_2-H	152.6	6.59	0.9610	(Wang et al., 2015)
	Fe_3O_4@SiO_2–NH_2	6.700	3.311	0.9696	(Zhang et al., 2013)
	PVP–SBA-15	2.143	1.37	0.964	(Betiha et al., 2020)
	Pb-IIMS-SBA-15	128.8	5.441	0.6674	(Cui et al., 2017)
	This work	148.7	3.83	0.95	-

Table 10. Kinetic parameters of Pb(II) adsorption with the $Fe_3O_4/SiO_2/KCC^{-1}$ nanocomposite

Model	Equation	Parameters	Value	$q_{e,exp}$.(mg g^{-1})
Pseudo-first order	$\log(q_e - q_t) = \log(q_e) - \frac{k_1 t}{2.303}$	k_1(min^{-1}) $q_{e,cal}$ (mg g^{-1}) R^2	0.14 490.2 0.99	494.2
Pseudo-second order	$\frac{t}{q_t} = \frac{1}{k_2 q_e^2} + \left(\frac{1}{q_e}\right) t$	k_2(g mg^{-1} min^{-1}) $q_{e,cal}$ (mg g^{-1}) R^2	3.38 540.5 0.98	

Where $q_{e,cal}$ (mg g^{-1}) is the adsorption capacity at equilibrium time, k_1 (min^{-1}) is the pseudo-first-order kinetic rate constant, k_2 (g mg^{-1} min^{-1}) is the pseudo-second-order kinetic rate constant.

the PSO[1] kinetic models, the removal process is based on physical adsorption and chemical adsorption, respectively.

Table 10 presents the kinetic parameters obtained from the two kinetic models. Comparing the PFO model with the PSO models in terms of R^2 values clearly indicated that the adsorption kinetics of Pb(II) came from a combination of both PFO and PSO kinetic models. However, the equilibrium adsorption capacity ($q_{e,cal}$) of $Fe_3O_4/SiO_2/KCC^{-1}$ calculated through the PFO model was closer to the experimental adsorption capacity ($q_{e,exp}$), a finding which indicated that the PFO model was more consistent with the experimental data than the PSO model. Hence, the PFO model played a more significant role.

Table 11 reports the kinetic parameters and correlation coefficients obtained from pseudo-first-order and pseudo-second-order models for the adsorption of

[1] Pseudo-Second-Order (PSO)

Table 11. Kinetic parameters of Pb(II) adsorption onto some mesoporous absorbents

Pseudo-first-order	Adsorbent	$q_{e,cal}$ (mg g^{-1})	k_1 (min^{-1})	R^2	Reference
	Fe_3O_4@SiO_2@m-SiO_2	281.68	0.04	0.998	(Javaheri et al., 2019)
	AS-ACI-2.0	75.5	0.11	0.996	(Zhou et al., 2018)
	PVP–SBA-15	25.59	0.04	0.998	(Betiha et al., 2020)
	MDA–SBA-15	52.30	0.11	0.986	(Shahbazi et al., 2011)
	This work	490.20	0.14	0.99	-
Pseudo-second-order	**Adsorbent**	**$q_{e,cal}$ (mg g^{-1})**	**k_2 (g mg^{-1} min^{-1})**	**R^2**	**Reference**
	Fe_3O_4@SiO_2@m-SiO_2	833.33	0.0008	0.616	(Javaheri et al., 2019)
	AS-ACI-2.0	78.3	0.0028	0.971	(Zhou et al., 2018)
	PVP–SBA-15	35.71429	0.00106	0.997	(Betiha et al., 2020)
	MDA–SBA-15	58.9	0.0025	0.955	(Shahbazi et al., 2011)
	This work	540.5	3.38	0.98	-

Pb(II) onto some mesoporous absorbents analyzed in previous studies. According to the results, the correlation coefficient (R^2) value of the pseudo-first-order kinetics model was higher than that of the pseudo-second-order kinetics model, a finding which indicated that the adsorption process of these composites for Pb(II) was more consistent with the pseudo-first-order kinetics. Moreover, the surface adsorption process was mainly physical.

3.8. Adsorption thermodynamics

Thermodynamic parameters reflect the feasibility and spontaneity of processes, endothermic or exothermic reactions, and entropy changes during a process. The thermodynamic parameters of Pb(II) adsorption onto $Fe_3O_4/SiO_2/KCC^{-1}$ include change in free energy (ΔG°), change in enthalpy (ΔH°), and change in entropy (ΔS°). These parameters were calculated through the variation of adsorbate distribution coefficient between the solid and liquid phases by using the following thermodynamic

equations (Eqs. 7, 8, and 9)

$$K_d = \frac{q_e}{C_e} \quad (7)$$

$$\ln K_d = \frac{\Delta H^\circ}{R}\frac{1}{T} + \frac{\Delta S^\circ}{R} \quad (8)$$

$$\Delta G^\circ = \Delta H^\circ - T\Delta S^\circ \quad (9)$$

Where

K_d refers to the dimensionless thermodynamic equilibrium constant for the adsorption process, and R denotes the ideal gas constant (8.314 J mol^{-1} K^{-1}). Moreover, T indicates the absolute temperature of the system (K), whereas q_e represents the equilibrium concentration of Pb(II) on the adsorbent surface (mg L^1), and C_e represents the concentration of Pb(II) in the solution (mg L^{-1}). After the thermodynamic equilibrium constant was calculated for different temperatures (through the Van 't Hoff equation), the ln K_d graph was plotted vs. 1/T (Equation 8). The values of ΔH° and ΔS° were then obtained from the slope and the intercept of the linear plot ln K_d vs. 1/T, respectively (Vij et al., 2021).

Moreover, the Gibbs free energy of the process at different temperatures was obtained from Equation 9. Table 12 reports the calculated values of ΔG°, ΔH°, and ΔS°. The negative ΔG° values at different temperatures indicate that the adsorption process of Pb(II) on $Fe_3O_4/SiO_2/KCC^{-1}$ was spontaneous, favorable, and feasible at all the studied temperatures. The increase in negative values of ΔG° with the increase in temperature indicated that adsorption was more favorable at higher temperatures (Table 12). This finding might be due to the hydration sheath of metal ions having to be destroyed before its sorption, a process which required energy (Guo et al., 2018). The Gibbs free energy ranging between 0 and -20 kJ mol^{-1} indicates physical absorption, whereas a range between -20 and -80 kJ mol^{-1} means chemical (or physical-chemical) adsorption (Samaniego et al., 2019).

In this study, the values of ΔG° indicated the physical adsorption of Pb(II) on the absorbent surface. Moreover, the positive ΔH° values (5.84 kJ mol^{-1}) denoted that the adsorption was naturally an endothermic process. As a result, according to Le Chatelier's principle, the progress

Table 12. Thermodynamic parameters for Pb(II) adsorption onto $Fe_3O_4/SiO_2/KCC^{-1}$ adsorbent in C_0= 10 mg L^{-1}

T(K)	q_e(mg g^{-1})	k_d(L g^{-1})	ΔG° (kJ mol^{-1})	ΔH° (kJ mol^{-1})	ΔS° (kJ mol^{-1} K^{-1})	R^2
293	2.50	0.67	-0.988	+5.84	+23.42	0.98
303	2.54	0.60	-1.272			
313	2.57	0.59	-1.520			
323	2.59	0.53	-1.717			
333	2.61	0.50	-1.930			

Table 13. Thermodynamic parameters for the adsorption of Pb(II) onto some mesoporous absorbents

Adsorbent	ΔH° (kJ mol^{-1})	ΔS° (J k^{-1} mol^{-1})	T (K)	ΔG° (kJ mol^{-1})	Reference
Cu-MOFs/Fe_3O_4	+28.76	+101.39	303 313	-2.47 -3.48	(Shi et al., 2018)
Fe_3O_4@SiO_2–NH_2	+18.05	+73.24	303 313	-4.53 -5.23	(Zhang et al., 2013)
AS-ACI-1.0	+31.81	+129.74	303 313	-7.52 -8.77	(Zhou et al., 2018)
SBA-16-G	+44.47	+0.21	303 313	-18.59 -19.66	(Gupta et al., 2019)
N-Fe/OMC	+39.13	+144.03	303 313	-5.97 -7.41	(Yang et al., 2015)
PMO-IL-SH	+25.01	98.48	303 313	-5.94 -6.04	(Elhamifar et al., 2016)
This work	+5.84	+23.42	303 313	-1.27 -1.52	-

Table 14. The removal of Pb(II) from various wastewater samples through synthesized adsorbent and the proposed method

Wastewater effluent	Added concentration (ng ml^{-1})	Removal (%)
Sample1	- 5 15	- 53% 62%
Sample2	- 5 15	- 46% 55%
Sample3	- 5 15	- 51% 60%

of the reaction increased as the temperature elevated; consequently, the adsorption capacity also increased. This finding is in agreement with the expected higher negative values of ΔG° at higher temperatures for endothermic adsorption. Previous studies on the adsorption of heavy metals reported that the heat in chemisorption and physisorption would fall into the ranges of 80–200 kJ mol^{-1} and 2.1–20.9 kJ mol^{-1}, respectively (Dinari et al., 2017, Soltani et al., 2019b, Soltani et al., 2019a, Liu and Liu, 2008).

Simultaneously, the positive values of ΔS° indicated an increase in the degree of freedom and randomness at the solid-solution boundary during the adsorption of Pb(II) onto $Fe_3O_4/SiO_2/KCC^{-1}$. In this situation, some internal structure changes may occur in the adsorbent. Furthermore, the positive value of ΔS° indicated the good affinity of the adsorbent for the Pb(II) ions. The thermodynamic study revealed the physical nature of adsorption with no structural alteration at the adsorbent–adsorbate interface. Table 13 reports the results of the thermodynamic study on the adsorption of Pb(II) onto some mesoporous absorbents. Accordingly, the values of ΔG° decreased as the temperature increased, a fact which indicated higher spontaneity at higher temperatures. At higher temperatures, lead ions are readily desolvated. Its diffusion through the medium and within the pores (intra-particle diffusion) would be a faster process contributing to the higher probability of lead adsorption

(Xin et al., 2012).

Moreover, the increase in the adsorption capacity of mesoporous adsorbents at higher temperatures can be caused by the enlargement of pore size and activation of the adsorbent surface (Masue et al., 2007).

3.9. Reusability and real wastewater treatment

In the actual treatment process, it is generally necessary to prepare excellent adsorbents with high desorption efficiency and good reusability to keep the cost at the lowest level. In this study, the capacity of the synthetic adsorbent for recycling and reusability for seven consecutive cycles were analyzed under the optimum conditions.

After the absorption process at each step, the adsorbent was separated from the Pb(II) solution by applying an external magnetic field. The Pb(II)-loaded adsorbent was then desorbed through a 2% (v/v) HNO_3 solution. After desorption, the adsorbents were regenerated with a 0.1 M NaOH solution, then washed to neutral with distilled water, and reused after heating to 150 $^{\circ}$C (Rott et al., 2018).

The regeneration study indicated that the adsorbent could be used for up to five cycles because the activity of the adsorbent and the absorption efficiency declined after the fifth cycle.

Three different petrochemical industry wastewater samples were utilized to evaluate the ability of $Fe_3O_4/SiO_2/KCC^{-1}$ magnetic composite in industrial wastewater treatment.

For this purpose, wastewater samples of the petrochemical industry were first filtered through a 0.45-µm Millipore membrane filter before the analysis to remove suspended particles and impurities. To analyze the effects of the sample matrices on the removal process, the samples were spiked by known concentrations of Pb(II) ions at two levels, 5 and 15 ng ml^{-1}. The proposed method was then implemented under optimal conditions.

According to Table 14, the maximum removal efficiency rates for the lead ions in the studied samples 1, 2, and 3 were reported 62%, 55%, and 60%, respectively.

These results indicated the optimal efficiency of the concerned adsorbent in the removal of Pb(II) ions from real wastewater. The high selectivity of synthesized adsorbent to target metal ions is still a challenge, which can encourage more efforts to functionalize adsorbent surfaces with desired chemical groups that can selectively bind specific metal ions.

4. Conclusion

In this study, a novel magnetic adsorbent ($Fe_3O_4/SiO_2/KCC^{-1}$) was successfully synthesized through a surfactant-templated microemulsion formation process. The high saturation magnetization (62.8 emu g^{-1}) of the prepared mesoporous adsorbent indicated easy and fast separation from water under a moderate magnetic field. The specific surface area of the mesoporous adsorbent was 835 m^2 g^{-1}, and the pore diameter was centered at around 2.5 nm. The independent factors (pH (A), adsorption dosage (B), contact time (C), and temperature (D)) in Pb(II) removal were optimized through the RSM combined with CCD. The optimal conditions were found at a pH of 5.6, a temperature of 80°C, an adsorbent dosage of 0.04 g L^{-1}, and a contact time of 38 min, with the predictable Pb(II) removal rate of 93.97% and the experimental Pb(II) removal rate of 90%. Temperature and pH were the most important parameters that affected Pb(II) adsorption on $Fe_3O_4/SiO_2/KCC^{-1}$. The isotherm study was best fitted with Langmuir's model, a finding which indicated that monolayer adsorption occurred on the surface of the homogenous adsorbent.

According to Langmuir's model, the maximum uptakes were reported 574.4 mg g^{-1}, a finding which was in good agreement with the maximum experimental uptake capacity (552.5 mg/g^{-1}). The resultant thermodynamic parameters indicated that the adsorption of Pb(II) on $Fe_3O_4/SiO_2/KCC^{-1}$ was spontaneous (negative values of ΔG°) and endothermic (positive values of ΔH°). In addition, the positive value of ΔS° suggested the increased randomness at the solid–liquid interphase during the adsorption of Pb(II) onto $Fe_3O_4/SiO_2/KCC^{-1}$. This adsorbent could be recovered and reused at least five times with no considerable decline in its performance.

In conclusion, the synthesized nanocomposite is a nontoxic, recoverable, and environmentally friendly adsorbent that can be used as an efficient adsorbent material for the removal of Pb(II) from an aqueous solution. The ability of these nanoparticles to transfer molecules fast due to their radial-like direct channels and large pore size together with their good adsorption capacity can make them promising materials for different applications such as water treatment and biomedical engineering.

5. Acknowledgements

The authors gratefully acknowledge the support of this work by the Islamic Azad University, Mashhad, Iran.

Reference

Abd Ali, L. I., Ibrahim, W. A. W., Sulaiman, A., Kamboh, M. A. & Sanagi, M. M. 2016. New chrysin-functionalized silica-core shell magnetic nanoparticles for the magnetic solid phase extraction of copper ions from water samples. *Talanta*, 148**,** 191-199.

Ahmad, S. Z. N., Salleh, W. N. W., Ismail, A. F., Yusof, N., Yusop, M. Z. M. & Aziz, F. 2020. Adsorptive removal of heavy metal ions using graphene-based nanomaterials: toxicity, roles of functional groups and mechanisms. *Chemosphere*, 248**,** 126008.

Alamri, H., AL-Shahrani, A., Bovero, E., Khaldi, T., Alabedi, G., Obaid, W., et al. 2018. Self-cleaning superhydrophobic epoxy coating based on fibrous silica-coated iron oxide magnetic nanoparticles. *Journal of Colloid and Interface Science*, 513**,** 349-356.

Anantha, M., Olivera, S., Hu, C., Jayanna, B., Reddy, N., Venkatesh, K., et al. 2020. Comparison of the photocatalytic, adsorption and electrochemical methods for the removal of cationic dyes from aqueous solutions. *Environmental Technology and Innovation*, 17**,** 100612.

Anbia, M., Kargosha, K. & Khoshbooei, S. 2015. Heavy metal ions removal from aqueous media by modified magnetic mesoporous silica MCM-48. *Chemical Engineering Research and Design*, 93**,** 779-788.

Abdollahi, S. N., Naderi, M. & Amoabediny, G. 2012. Synthesis and physicochemical characterization of tunable silica–gold nanoshells via seed growth method. *Colloids and Surfaces A: Physicochemical and Engineering Aspects*, 414**,** 345-351.

Awual, M. R. 2019. Mesoporous composite material for efficient lead (II) detection and removal from aqueous media. *Journal of Environmental Chemical Engineering*, 7**,** 103124.

Awual, M. R., Hasan, M. M. & Shahat, A. 2014. Functionalized novel mesoporous adsorbent for selective lead (II) ions monitoring and removal from wastewater. *Sensors and Actuators B: Chemical*, 203**,** 854-863.

Asuquo, E., Martin, A., Nzerem, P., Siperstein, F. & Fan, X. 2017. Adsorption of Cd(II) and Pb(II) ions from aqueous solutions using mesoporous activated carbon adsorbent: equilibrium, kinetics and characterisation studies. *Journal of Environmental Chemical Engineering,* 5**,** 679-698.

Bao, S., Li, K., Ning, P., Peng, J., Jin, X. & Tang, L. 2017. Highly effective removal of mercury and lead ions from wastewater by mercaptoamine-functionalised silica-coated magnetic nano-adsorbents: behaviours and mechanisms. *Applied Surface Science*, 393**,** 457-466.

Bayuo, J., Abukari, M. A. & Pelig-Ba, K. B. 2020. Optimization using central composite design (CCD) of response surface methodology (RSM) for biosorption of hexavalent chromium from aqueous media. *Applied Water Science*, 10**,** 1-12.

Betiha, M. A., Moustafa, Y. M., EL-Shahat, M. F. & Rafik, E. 2020. Polyvinylpyrrolidone-Aminopropyl-SBA-15 schiff Base hybrid for efficient removal of divalent heavy metal cations from wastewater. *Journal of Hazardous Materials*, 397**,** 122675.

Bhattacharya, S. 2021. Central composite design for response surface methodology and its application in pharmacy. In: Kayaroganam, P., *Response Surface Methodology in Engineering Science*. IntechOpen, India.

Cao, Y., Khan, A., Kurniawan, T. A., Soltani, R. & Albadarin, A. B. 2021. Synthesis of hierarchical micro-mesoporous LDH/MOF nanocomposite with in situ growth of UiO-66-(NH_2) 2 Mof on the functionalized NiCo-LDH ultrathin sheets and its application for thallium (I) removal. *Journal of Molecular Liquids*, 336**,** 116189.

Cheng, S., Zhao, S., Guo, H., Xing, B., Liu, Y., Zhang, C. 2022. High-efficiency removal of lead/cadmium from wastewater by MgO modified biochar derived from crofton weed. *Bioresource Technology*, 343**,** 126081.

Cheraghipour, E. & Pakshir, M. 2020. Process optimization and modeling of Pb(II) ions adsorption on chitosan-conjugated magnetite nano-biocomposite using response surface methodology. *Chemosphere*, 260**,** 127560.

Clifford, D., Subramonian, S. & Sorg, T. J. 1986. Water treatment processes. III. Removing dissolved inorganic contaminants from water. *Environmental Science and Technology*, 20**,** 1072-1080.

Cui, H. Z., Li, Y. L., Liu, S., Zhang, J. F., Zhou, Q., Zhong, R., et al. 2017. Novel Pb(II) ion-imprinted materials based on bis-pyrazolyl functionalized mesoporous silica for the selective removal of Pb(II) in water samples. *Microporous and Mesoporous Materials*, 241**,** 165-177.

Da'na, E. & Sayari, A. 2012. Adsorption of heavy metals on amine-functionalized SBA-15 prepared by co-condensation: applications to real water samples. *Desalination*, 285**,** 62-67.

Dahlan, I., Azhar, E. E. M., Hassan, S. R., Aziz, H. A. & Hung, Y. T. 2022. Statistical modeling and optimization of process parameters for 2, 4-dichlorophenoxyacetic acid removal by using AC/PDMAEMA hydrogel adsorbent: comparison of different RSM designs and ANN training methods. *Water*, 14**,** 3061.

Dan, S., Kalantari, M., Kamyabi, A. & Soltani, M. 2021. Synthesis of chitosan-g-itaconic acid hydrogel as an antibacterial drug carrier: optimization through RSM-CCD. *Polymer Bulletin*, 1-24.

Dao, T. U. T., Nguyen, H. T. T., Nguyen, D. T. C., Le, H. T., Nguyen, H. T., Do, S. T., et al. 2020. Process optimization studies of Congo Red dye adsorption onto magnesium aluminium layered double hydroxide using response surface methodology. *Polish Journal of Environmental Studies*, 30**,** 679-687.

Dehghani, M. H., Karri, R. R., Yeganeh, Z. T., Mahvi, A. H., Nourmoradi, H., Salari, M., et al. 2020. Statistical modelling of endocrine disrupting compounds adsorption onto activated carbon prepared from wood using CCD-RSM and DE hybrid evolutionary optimization framework: comparison of linear vs non-linear isotherm and kinetic parameters. *Journal of Molecular Liquids*, 302**,** 112526.

Dhaliwal, S. S., Singh, J., Taneja, P. K. & Mandal, A. 2020. Remediation techniques for removal of heavy metals from the soil contaminated through different sources: a review. *Environmental Science and Pollution Research*, 27**,** 1319-1333.

Dinari, M., Soltani, R. & Mohammadnezhad, G. 2017. Kinetics and thermodynamic study on novel modified–mesoporous silica MCM-41/polymer matrix nanocomposites: effective adsorbents for trace CrVI removal. *Journal of Chemical and Engineering Data*, 62**,** 2316-2329.

Ding, H., Zhang, Y., Wang, S., Xu, J., Xu, S. & Li, G. 2012. Fe_3O_4@ SiO_2 core/shell nanoparticles: the silica coating regulations with a single core for different core sizes and shell thicknesses. *Chemistry of Materials*, 24**,** 4572-4580.

Eltaweil, A., Mohamed, H. A., Abd EL-Monaem, E. M. & EL-Subruiti, G. 2020. Mesoporous magnetic biochar composite for enhanced adsorption of malachite green dye: characterization, adsorption kinetics, thermodynamics and isotherms. *Advanced Powder Technology*, 31**,** 1253-1263.

Elhamifar, D., Shojaeipoor, F. & Yari, O. 2016. Thiopropyl-containing ionic liquid based periodic mesoporous organosilica as a novel and efficient adsorbent for the removal of Hg (II) and Pb(II) ions from aqueous solutions. *RSC Advances*, 6**,** 58658-58666.

Faraji-Khiavi, F., Jalilian, H., Heydari, S., Sadeghi, R., Saduqi, M., Razavinasab, S. A., et al. 2022. Utilization of health services among the elderly in Iran during the COVID-19 outbreak: a cross-sectional study. *Health Science Reports*, 5**,** e839.

Fattahi, M., Ezzatzadeh, E., Jalilian, R. & Taheri, A. 2021. Micro solid phase extraction of cadmium and lead on a new ion-imprinted hierarchical mesoporous polymer via dual-template method in river water and fish muscles: optimization by experimental design. *Journal of Hazardous Materials*, 403**,** 123716.

Fiyadh, S. S., Alsaadi, M. A., Jaafar, W. Z., Alomar, M. K., Fayaed, S. S., Mohd, N. S., et al. 2019. Review on heavy metal adsorption processes by carbon nanotubes. *Journal of Cleaner Production*, 230**,** 783-793.

Fooladgar, S., Teimouri, A. & Ghanavati Nasab, S. 2019. Highly efficient removal of lead ions from aqueous solutions using chitosan/rice husk ash/nano alumina with a focus on optimization by response surface methodology: isotherm, kinetic, and thermodynamic studies. *Journal of Polymers and the Environment*, 27**,** 1025-1042.

Guo, T., Bulin, C., Li, B., Zhao, Z., Yu, H., Sun, H., et al. 2018. Efficient removal of aqueous Pb(II) using partially reduced graphene oxide-Fe_3O_4. *Adsorption Science and Technology*, 36**,** 1031-1048.

Gupta, R., Gupta, S. K. & Pathak, D. D. 2019. Selective adsorption of toxic heavy metal ions using guanine-functionalized mesoporous silica [SBA-16-g] from aqueous solution. *Microporous and Mesoporous Materials*, 288**,** 109577.

Hasan, R., Chong, C., Bukhari, S., Jusoh, R. & Setiabudi, H. 2019. Effective removal of Pb(II) by low-cost fibrous silica KCC^{-1} synthesized from silica-rich rice husk ash. *Journal of Industrial and Engineering Chemistry*, 75**,** 262-270.

Hasan, R. & Setiabudi, H. 2019. Removal of Pb(II) from aqueous solution using KCC^{-1}: optimization by response surface methodology (RSM). *Journal of King Saud University-Science*, 31**,** 1182-1188.

Hassan, M., Naidu, R., Du, J., Qi, F., Ahsan, M. A. & Liu, Y. 2022. Magnetic responsive mesoporous alginate/β-cyclodextrin polymer beads enhance selectivity and adsorption of heavy metal ions. *International Journal of Biological Macromolecules*, 207**,** 826-840.

He, H., Meng, X., Yue, Q., Yin, W., Gao, Y., Fang, P., et al. 2021. Thiol-ene click chemistry synthesis of a novel magnetic mesoporous silica/chitosan composite for selective Hg(II) capture and high catalytic activity of spent Hg(II) adsorbent. *Chemical Engineering Journal*, 405**,** 126743.

Hao, Y. M., Man, C. & Hu, Z. B. 2010. Effective removal of Cu(II) ions from aqueous solution by amino-functionalized magnetic nanoparticles. *Journal of Hazardous Material*s, 184**,** 392-399.

Heidari, A., Younesi, H. & Mehraban, Z. 2009. Removal of Ni(II), Cd(II), and Pb(II) from a ternary aqueous solution by amino functionalized mesoporous and nano mesoporous silica. *Chemical Engineering Journal*, 153**,** 70-79.

Huang, J., Ye, M., Qu, Y., Chu, L., Chen, R., He, Q. & Xu, D. 2012. Pb(II) removal from aqueous media by EDTA-modified mesoporous silica SBA-15. *Journal of Colloid and Interface Science*, 385**,** 137-146.

Izgi, M. S., Ece, M. Ş., Kazici, H. Ç. K., Şahin, Ö. & Onat, E. 2020. Hydrogen production by using Ru nanoparticle decorated with Fe_3O_4@ SiO_2–NH_2 core-shell microspheres. *International Journal of Hydrogen Energy*, 45**,** 30415-30430.

Javaheri, F., Kheshti, Z., Ghasemi, S. & Altaee, A. 2019. Enhancement of Cd^{2+} removal from aqueous solution by multifunctional mesoporous silica: equilibrium isotherms and kinetics study. *Separation and Purification Technology*, 224**,** 199-208.

Javadian, H., Koutenaei, B. B., Shekarian, E., Sorkhrodi, F. Z., Khatti, R. & Toosi, M. 2017. Application of functionalized nano HMS type mesoporous silica with N-(2-aminoethyl)-3-aminopropyl methyldimethoxysilane as a suitable adsorbent for removal of Pb(II) from aqueous media and industrial wastewater. *Journal of Saudi Chemical Society*, 21**,** S219-S230.

Janighorban, M., Rasouli, N., Sohrabi, N. & Ghaedi, M. 2020. Response surface methodology for optimizing Cd(II) adsorption onto a novel chemically changed nano Zn_2Al-layer double hydroxide. *Advanced Journal of Chemistry Section A*, 3**,** 701.

Jin, X., Li, K., Ning, P., Bao, S. & Tang, L. 2017. Removal of Cu(II) ions from aqueous solution by magnetic chitosan-tripolyphosphate modified silica-coated adsorbent: characterization and mechanisms. *Water, Air and Soil Pollution*, 228**,** 1-14.

Joshi, S., Bajpai, S. & Jana, S. 2020. Application of ANN and RSM on fluoride removal using chemically activated D. sissoo sawdust. *Environmental Science and Pollution Research*, 27**,** 17717-17729.

Khan, S. U., Farooqi, I. H., Usman, M. & Basheer, F. 2020. Energy efficient rapid removal of arsenic in an electrocoagulation reactor with hybrid Fe/Al electrodes: process optimization using CCD and kinetic modeling. *Water*, 12**,** 2876.

Khan, S. U., Mahtab, M. S. & Farooqi, I. H. 2021. Enhanced lead (II) removal with low energy consumption in an electrocoagulation column employing concentric electrodes: process optimisation by RSM using CCD. *International Journal of Environmental Analytical Chemistry*, 1-18.

Lapwanit, S., Trakulsujaritchok, T. & Nongkhai, P. N. 2016. Chelating magnetic copolymer composite modified by click reaction for removal of heavy metal ions from aqueous solution. *Chemical Engineering Journal*, 289**,** 286-295.

Li, S., Li, S., Wen, N., Wei, D. & Zhang, Y. 2021. Highly effective removal of lead and cadmium ions from wastewater by bifunctional magnetic mesoporous silica. *Separation and Purification Technology*, 265**,** 118341.

Li, Z., Tang, X., Liu, K., Huang, J., Peng, Q., Ao, M., et al. 2018. Fabrication of novel sandwich nanocomposite as an efficient and regenerable adsorbent for methylene blue and Pb(II) ion removal. *Journal of Environmental Management*, 218**,** 363-373.

Li, G., Zhao, Z., Liu, J. & Jiang, G. 2011a. Effective heavy metal removal from aqueous systems by thiol functionalized magnetic mesoporous silica. *Journal of Hazardous Materials*, 192**,** 277-283.

Li, W., Deng, Y., Wu, Z., Qian, X., Yang, J., Wang, Y., et al. 2011b. Hydrothermal etching assisted crystallization: a facile route to functional yolk-shell titanate microspheres with ultrathin nanosheets-assembled double shells. *Journal of the American Chemical Society*, 133**,** 15830-15833.

Liu, Y., Fu, R., Sun, Y., Zhou, X., Baig, S. A. & Xu, X. 2016. Multifunctional nanocomposites Fe_3O_4@ SiO_2-EDTA for Pb(II) and Cu (II) removal from aqueous solutions. *Applied Surface Science*, 369**,** 267-276.

Liu, Y. & Liu, Y. J. 2008. Biosorption isotherms, kinetics and thermodynamics. *Separation and Purification Technology*, 61**,** 229-242.

Liu, Z., Haddad, M., Sauve, S. & Barbeau, B. 2021. Alleviating the burden of ion exchange brine in water treatment: from operational strategies to brine management. *Water Research*, 205**,** 117728.

Manzar, M. S., Khan, G., Dos Santos Lins, P. V., Zubair, M., Khan, S. U., Selvasembian, R., et al. 2021. RSM-CCD optimization approach for the adsorptive removal of Eriochrome Black T from aqueous system using steel slag-based adsorbent: characterization, isotherm, kinetic modeling and thermodynamic analysis. *Journal of Molecular Liquids*, 339**,** 116714.

Masue, Y., Loeppert, R. H. & Kramer, T. A. 2007. Arsenate and arsenite adsorption and desorption behavior on coprecipitated aluminum: iron hydroxides. *Environmental Science and Technology*, 41**,** 837-842.

Moghaddam, S. S., Moghaddam, M. A. & Arami, M. 2010. Coagulation/flocculation process for dye removal using sludge from water treatment plant: optimization through response surface methodology. *Journal of Hazardous Materials*, 175**,** 651-657.

Moosazade, M., Ashoori, R., Moghimi, H., Amani, M. A., Frontistis, Z. & Taheri, R. A. 2021. Electrochemical recovery to overcome direct osmosis concentrate-bearing lead: optimization of treatment process via RSM-CCD. *Water*, 13**,** 3136.

Mehdinia, A., Shegefti, S. & Shemirani, F. 2015. Removal of lead(II), copper(II) and zinc(II) ions from aqueous solutions using magnetic amine-functionalized mesoporous silica nanocomposites. *Journal of the Brazilian Chemical Society*, 26**,** 2249-2257.

Monier, M., Ayad, D., Wei, Y. & Sarhan, A. 2010. Adsorption of Cu (II), Co (II), and Ni (II) ions by modified magnetic chitosan chelating resin. *Journal of Hazardous Materials*, 177**,** 962-970.

Narayan, R., Nayak, U. Y., Raichur, A. M. & Garg, S. 2018. Mesoporous silica nanoparticles: a comprehensive review on synthesis and recent advances. *Pharmaceutics*, 10**,** 118.

Nasab, S. G., Semnani, A., Karimi, M., Yazd, M. J. & Cheshmekhezr, S. 2019. Synthesis of ion-imprinted polymer-decorated SBA-15 as a selective and efficient system for the removal and extraction of Cu(II) with focus on optimization by response surface methodology. *Analyst*, 144**,** 4596-4612.

Nowicka, A., Kucharska, A. Z., Sokół-Łętowska, A. & Fecka, I. 2019. Comparison of polyphenol content and antioxidant capacity of strawberry fruit from 90 cultivars of Fragaria× ananassa Duch. *Food Chemistry*, 270**,** 32-46.

Polshettiwar, V., Cha, D., Zhang, X. & Basset, J. M. 2010. High-surface-area silica nanospheres (KCC^{-1}) with a fibrous morphology. *Angewandte Chemie International Edition*, 49**,** 9652-9656.

Pongsumpun, P., Iwamoto, S. & Siripatrawan, U. 2020. Response surface methodology for optimization of cinnamon essential oil nanoemulsion with improved stability and antifungal activity. *Ultrasonics Sonochemistry*, 60**,** 104604.

Rahimi, T., Kahrizi, D., Feyzi, M., Ahmadvandi, H. R. & Mostafaei, M. 2021. Catalytic performance of MgO/Fe_2O_3-SiO_2 core-shell magnetic nanocatalyst for biodiesel production of Camelina sativa seed oil: Optimization by RSM-CCD method. *Industrial Crops and Products*, 159**,** 113065.

Razmi, F. A., Ngadi, N., Wong, S., Inuwa, I. M. & Opotu, L. A. 2019. Kinetics, thermodynamics, isotherm and regeneration analysis of chitosan modified pandan adsorbent. *Journal of Cleaner Production*, 231**,** 98-109.

Reddy, K. R., Gomes, V. G. & Hassan, M. 2014. Carbon functionalized TiO_2 nanofibers for high efficiency photocatalysis. *Materials Research Express*, 1**,** 015012.

Rott, E., Nouri, M., Meyer, C., Minke, R., Schneider, M., Mandel, K., et al. 2018. Removal of phosphonates from synthetic and industrial wastewater with reusable magnetic adsorbent particles. *Water Research*, 145**,** 608-617.

Salman, D., Juzsakova, T., Al-Mayyahi, M., Ákos, R., Mohsen, S., Ibrahim, R., et al. 2021. Synthesis, surface modification and characterization of magnetic Fe_3O_4@ SiO_2 core-shell nanoparticles. *Journal of Physics: Conference Series*. IOP Publishing, 012039.

Samaniego, M. L., De Luna, M. D. G., Ong, D. C., Wan, M. W. & Lu, M. C. 2019. Isotherm and thermodynamic studies on the removal of sulfur from diesel fuel by mixing-assisted oxidative–adsorptive desulfurization technology. *Energy and Fuels*, 33**,** 1098-1105.

Šćiban, M., Klašnja, M. & Škrbić, B. 2006. Modified softwood sawdust as adsorbent of heavy metal ions from water. *Journal of Hazardous Materials*, 136**,** 266-271.

Singh, B. & Polshettiwar, V. 2016. Design of CO_2 sorbents using functionalized fibrous nanosilica (KCC^{-1}): insights into the effect of the silica morphology (KCC^{-1} vs. MCM-41). *Journal of Materials Chemistry A*, 4**,** 7005-7019.

Soltani, R., Dinari, M. & Mohammadnezhad, G. 2018. Ultrasonic-assisted synthesis of novel nanocomposite of poly (vinyl alcohol) and amino-modified MCM-41: a green adsorbent for Cd(II) removal. *Ultrasonics Sonochemistry*, 40**,** 533-542.

Soltani, R., Marjani, A. & Shirazian, S. 2019a. Facile one-pot synthesis of thiol-functionalized mesoporous silica submicrospheres for Tl(I) adsorption: isotherm, kinetic and thermodynamic studies. *Journal of Hazardous Materials*, 371**,** 146-155.

Soltani, R., Marjani, A. & Shirazian, S. 2019b. Shell-in-shell monodispersed triamine-functionalized SiO_2 hollow microspheres with micro-mesostructured shells for highly efficient removal of heavy metals from aqueous solutions. *Journal of Environmental Chemical Engineering*, 7**,** 102832.

Soltani, R., Marjani, A., Soltani, R. & Shirazian, S. 2020. Hierarchical multi-shell hollow micro–meso–macroporous silica for Cr(VI) adsorption. *Scientific Reports*, 10**,** 1-12.

Sun, D., Zhao, Y., Cao, Y., Liu, M., Zhang, Y., Zhao, L., et al. 2020. Investigation on the interaction mechanism of the solvent extraction for mercaptan removal from liquefied petroleum gas. *Energy and Fuels*, 34**,** 4788-4798.

Sun, Z., Cui, G., Li, H., Liu, Y., Tian, Y. & Yan, S. 2016. Multifunctional optical sensing probes based on organic–inorganic hybrid composites. *Journal of Materials Chemistry B,* 4**,** 5194-5216.

Shahbazi, A., Younesi, H. & Badiei, A. 2011. Functionalized SBA-15 mesoporous silica by melamine-based dendrimer amines for adsorptive characteristics of Pb(II), Cu(II) and Cd(II) heavy metal ions in batch and fixed bed column. *Chemical Engineering Journal*, 168**,** 505-518.

Shi, Z., Xu, C., Guan, H., Li, L., Fan, L., Wang, Y., et al. 2018. Magnetic metal organic frameworks (MOFs) composite for removal of lead and malachite green in wastewater. *Colloids and Surfaces A: Physicochemical and Engineering Aspects*, 539**,** 382-390.

Saeidi, N., Parvini, M. & Niavarani, Z. 2015. High surface area and mesoporous graphene/activated carbon composite for adsorption of Pb(II) from wastewater. *Journal of Environmental Chemical Engineering*, 3**,** 2697-2706.

Taseidifar, M., Ziaee, M., Pashley, R. M. & Ninham, B. W. 2019. Ion flotation removal of a range of contaminant ions from drinking water. *Journal of Environmental Chemical Engineering*, 7**,** 103263.

Topal, M. & Topal, E. I. A. 2020. Optimization of tetracycline removal with chitosan obtained from mussel shells using RSM. *Journal of Industrial and Engineering Chemistry*, 84**,** 315-321.

Torğut, G., Tanyol, M. & Meşe, Z. 2020. Modeling and optimization of indigo carmine adsorption from aqueous solutions using a novel polymer adsorbent: RSM-CCD. *Chemical Engineering Communications*, 207**,** 1157-1170.

Venkateswarlu, S., Kumar, B. N., Prathima, B., Subbarao, Y. & Jyothi, N. V. V. 2019. A novel green synthesis of Fe_3O_4 magnetic nanorods using Punica Granatum rind extract and its application for removal of Pb(II) from aqueous environment. *Arabian Journal of Chemistry*, 12**,** 588-596.

Vickers, N. J. 2017. Animal communication: when i'm calling you, will you answer too? *Current Biology*, 27**,** R713-R715.

Vieira, W. T., De Farias, M. B., Spaolonzi, M. P., DA Silva, M. G. C. & Vieira, M. G. A. 2020. Removal of endocrine disruptors in waters by adsorption, membrane filtration and biodegradation. a review. *Environmental Chemistry Letters*, 18**,** 1113-1143.

Vij, R. K., Janani, V. A., Subramanian, D., Mistry, C. R., Devaraj, G. & Pandian, S. 2021. Equilibrium, kinetic and thermodynamic studies for the removal of Reactive Red dye 120 using Hydrilla verticillata biomass: a batch and column study. *Environmental Technology and Innovation*, 24**,** 102009.

Vojoudi, H., Badiei, A., Bahar, S., Ziarani, G. M., Faridbod, F. & Ganjali, M. R. 2017. A new nano-sorbent for fast and efficient removal of heavy metals from aqueous solutions based on Modification of magnetic mesoporous silica nanospheres. *Journal of Magnetism and Magnetic Materials*, 441**,** 193-203.

Wang, J., Tong, X., Chen, Y., Sun, T., Liang, L. & Wang, C. 2020a. Enhanced removal of Cr(III) in high salt organic wastewater by EDTA modified magnetic mesoporous silica. *Microporous and Mesoporous Materials*, 303**,** 110262.

Wang, N., Yang, D., Wang, X., Yu, S., Wang, H., Wen, T., et al. 2018. Highly efficient Pb(II) and Cu(II) removal using hollow Fe_3O_4@ PDA nanoparticles with excellent application capability and reusability. *Inorganic Chemistry Frontiers*, 5**,** 2174-2182.

Wang, P., Shen, T., Li, X., Tang, Y. & Li, Y. 2020b. Magnetic mesoporous calcium carbonate-based nanocomposites for the removal of toxic Pb(II) and Cd(II) ions from water. *ACS Applied Nano Materials*, 3**,** 1272-1281.

Wu, Y., Pang, H., Liu, Y., Wang, X., Yu, S., Fu, D., et al. 2019. Environmental remediation of heavy metal ions by novel-nanomaterials: a review. *Environmental Pollution*, 246**,** 608-620.

Wang, L., Sun, Y., Wang, J., Wang, J., Yu, A., Zhang, H., et al. 2011. Preparation of surface plasmon resonance biosensor based on magnetic core/shell Fe_3O_4/SiO_2 and $Fe_3O_4/Ag/SiO_2$ nanoparticles. *Colloids and Surfaces B: Biointerfaces*, 84**,** 484-490.

Wang, S., Wang, K., Dai, C., Shi, H. & Li, J. 2015. Adsorption of Pb^{2+} on amino-functionalized core–shell magnetic mesoporous SBA-15 silica composite. *Chemical Engineering Journal*, 262**,** 897-903.

Xin, X., Wei, Q., Yang, J., Yan, L., Feng, R., Chen, et al. 2012. Highly efficient removal of heavy metal ions by amine-functionalized mesoporous Fe_3O_4 nanoparticles. *Chemical Engineering Journal*, 184**,** 132-140.

Wu, X. W., Ma, H. W., Yang, J., Wang, F. J. & Li, Z. H. 2012. Adsorption of Pb(II) from aqueous solution by a poly-elemental mesoporous adsorbent. *Applied Surface Science*, 258**,** 5516-5521.

Xu, J., Cao, Z., Zhang, Y., Yuan, Z., Lou, Z., Xu, X., et al. 2018. A review of functionalized carbon nanotubes and graphene for heavy metal adsorption from water: preparation, application, and mechanism. *Chemosphere*, 195**,** 351-364.

Xu, P., Wang, H., Tong, R., Du, Q. & Zhong, W. 2006. Preparation and morphology of SiO_2/PMMA nanohybrids by microemulsion polymerization. *Colloid and Polymer Science*, 284**,** 755-762.

Xu, Z., Feng, Y., Liu, X., Guan, M., Zhao, C. & Zhang, H. 2010. Synthesis and characterization of Fe_3O_4@ SiO_2@ poly-l-alanine, peptide brush–magnetic microspheres through NCA chemistry for drug delivery and enrichment of BSA. *Colloids and Surfaces B: Biointerfaces*, 81**,** 503-507.

Yang, S., Zong, P., Ren, X., Wang, Q. & Wang, X. 2012. Rapid and highly efficient preconcentration of Eu(III) by core–shell structured Fe_3O_4@ humic acid magnetic nanoparticles. *ACS Applied Materials and Interfaces*, 4**,** 6891-6900.

Yang, G., Tang, L., Zeng, G., Cai, Y., Tang, J., Pang, Y., et al. 2015. Simultaneous removal of lead and phenol contamination from water by nitrogen-functionalized magnetic ordered mesoporous carbon. *Chemical Engineering Journal*, 259**,** 854-864.

Yu, K., Zhang, X., Tong, H., Yan, X. & Liu, S. 2013. Synthesis of fibrous monodisperse core–shell $Fe_3O_4/SiO_2/KCC^{-1}$. *Materials Letters*, 106**,** 151-154.

Yuna, Z. 2016. Review of the natural, modified, and synthetic zeolites for heavy metals removal from wastewater. *Environmental Engineering Science*, 33**,** 443-454.

Zhang, F., Shi, Y., Zhao, Z., Ma, B., Wei, L. & Lu, L. 2014. Amino-functionalized Fe_3O_4/SiO_2 magnetic submicron composites and In 3^+ ion adsorption properties. *Journal of Materials Science*, 49**,** 3478-3483.

Zhang, J., Zhai, S., Li, S., Xiao, Z., Song, Y., An, Q., et al. 2013. Pb(II) removal of Fe_3O_4@ SiO_2–NH_2 core–shell nanomaterials prepared via a controllable sol–gel process. *Chemical Engineering Journal*, 215**,** 461-471.

Zhao, W., Cui, B., Peng, H., Qiu, H. & Wang, Y. 2015. Novel method to investigate the interaction force between etoposide and APTES-functionalized Fe_3O_4@nSiO_2@ mSiO_2 nanocarrier for drug loading and release processes. *The Journal of Physical Chemistry C*, 119**,** 4379-4386.

Zhou, J., Liu, Y., Zhou, X., Ren, J. & Zhong, C. 2018. Magnetic multi-porous bio-adsorbent modified with amino siloxane for fast removal of Pb(II) from aqueous solution. *Applied Surface Science*, 427**,** 976-985.